A structural model for the South Tibetan detachment system in northwestern Bhutan from integration of temperature, fabric, strain, and kinematic data

Sean P. Long[1,*], Connor L. Mullady[1], Jesslyn K. Starnes[1], Stacia M. Gordon[2], Kyle P. Larson[3], Laura S. Pianowski[1], Robert B. Miller[4], and Emmanuel Soignard[5]

[1]SCHOOL OF THE ENVIRONMENT, WASHINGTON STATE UNIVERSITY, PULLMAN, WASHINGTON 99164, USA
[2]DEPARTMENT OF GEOLOGICAL SCIENCES AND ENGINEERING, UNIVERSITY OF NEVADA, RENO, NEVADA 89557, USA
[3]DEPARTMENT OF EARTH AND ENVIRONMENTAL SCIENCES, UNIVERSITY OF BRITISH COLUMBIA OKANAGAN, KELOWNA, BRITISH COLUMBIA, CANADA
[4]GEOLOGY DEPARTMENT, SAN JOSE STATE UNIVERSITY, SAN JOSE, CALIFORNIA 95192, USA
[5]LEROY EYRING CENTER FOR SOLID STATE SCIENCE, ARIZONA STATE UNIVERSITY, TEMPE, ARIZONA 85287, USA

ABSTRACT

Despite playing a fundamental role in all models of Himalayan tectonics, minimal data constraining the structural evolution, metamorphic history, and offset magnitude of the South Tibetan detachment system (STDS) are available. Here, we integrate petrofabric, finite strain, and kinematic data with metamorphic and deformation temperatures to generate a structural model for the STDS in northwestern Bhutan. We divide the STDS into an ~2-km-thick lower level that accommodated ~6–13 km of thinning via ≥30–76 km of simple shear-dominant displacement within Greater Himalayan rocks, and an ~3-km-thick upper level that accommodated ≥21 km of displacement via an upward decrease (from 44% to 2%) in transport-parallel lengthening within Tethyan Himalayan rocks. Peak metamorphic temperatures in the lower level are ~650–750 °C, and two distinct intervals of telescoped isotherms in the upper level define a cumulative upward decrease from ~700 to ~325 °C. These intervals are separated by an abrupt upward increase from ~450 to ~620 °C, which we interpret as the result of post-STDS thrust repetition. Above the upper telescoped interval, temperatures gradually decrease upward from ~325 to ~250 °C through a 7-km-thick section of overlying Tethyan Himalayan rocks. Telescoped isotherms lie entirely above the high-strain lower level of the STDS zone, which we attribute to progressive elevation of isotherms during protracted intrusion of granite sills. This study demonstrates the utility of using gradients in fabric intensity and thin section-scale finite strain to delineate shear zone boundaries when field criteria for delineating strain gradients are not apparent.

INTRODUCTION

One of the most intriguing and enigmatic aspects of the structural architecture of the Himalayan orogen is the "metamorphic sandwich" of high-grade metasedimentary and igneous rocks of the Greater Himalayan (GH) package, which are situated between lower-grade metasedimentary rocks above and below (e.g., Yin, 2006; Kohn, 2014). At the top of the GH package, the top-to-north South Tibetan Detachment system (STDS) of normal faults and shear zones separates migmatitic GH rocks, which were deformed at mid-crustal levels, from overlying low-grade to un-metamorphosed, upper-crustal sedimentary rocks of the Tethyan Himalayan (TH) package (Fig. 1) (e.g., Burg and Chen, 1984; Herren, 1987; Burchfiel et al., 1992; Hodges et al., 1992; Godin et al., 2006; Kellett et al., 2018). Since its recognition, the STDS has become a key focus of Himalayan research, primarily for the kinematic challenge that it presents, requiring north-vergent displacement during construction of an overall south-vergent contractional orogenic belt. The STDS remains the most controversial first-order structure in the orogen, and plays an important (but widely varying) role in virtually every model of Himalayan orogenesis. For example, earlier studies attributed motion on the STDS to rotation of principal stress directions as a result of the topographic gradient between India and Tibet (Burchfiel and Royden, 1985), or as a consequence of surface uplift combined with cessation of slip on the underlying Main Central thrust (England and Molnar, 1993). More recently, the STDS has been interpreted as a structure that helped accommodate high-magnitude southward extrusion of a mid-crustal channel composed of GH rocks (e.g., Grujic et al., 1996; Beaumont et al., 2001; 2004; Jamieson et al., 2004), a normal fault system generated within an orogenic wedge governed by critical taper dynamics (e.g., Robinson et al., 2003, 2006; Kohn, 2008), a structure related to the dynamics of translation and structural thickening of the underlying GH section (Cottle et al., 2015; Larson et al., 2015), or as a backthrust system bounding the top of a southward-propagating tectonic wedge (Webb et al., 2007, 2011; He et al., 2015).

A critical prerequisite for interpreting the genesis of the STDS is an understanding of the structural and metamorphic field gradients that are the cumulative result of north-vergent shearing, and the implications of these gradients for offset magnitude. To date, few studies have documented the

Sean P. Long ⓘ http://orcid.org/0000-0001-6548-9394
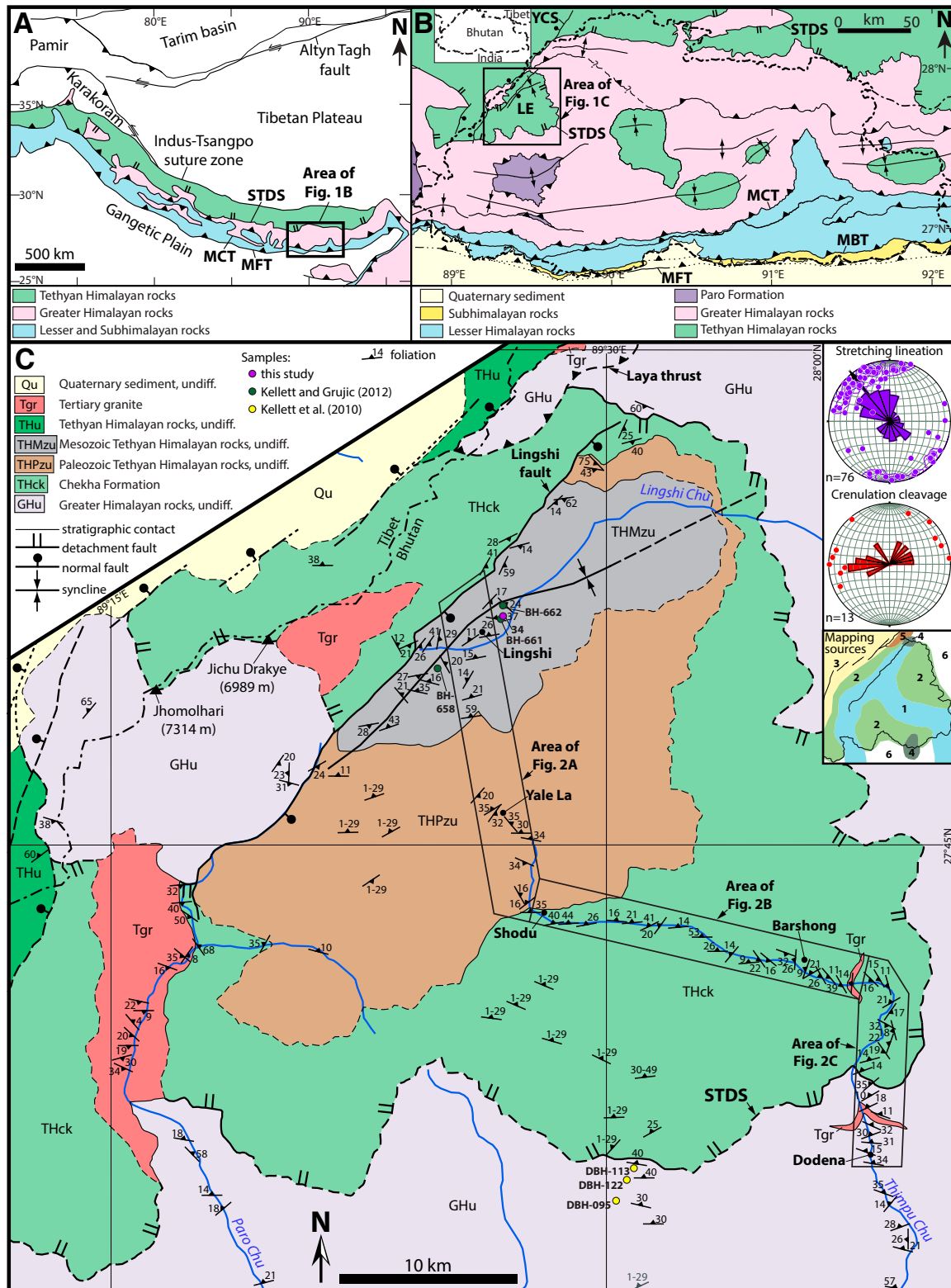*Corresponding author: sean.p.long@wsu.edu

Figure 1. (A) Generalized geologic map of the Himalayan-Tibetan orogen (simplified from Yin, 2006). (B) Simplified geologic map of Bhutan (modified from Long et al., 2017). MFT—Main Frontal thrust; MBT—Main Boundary thrust; MCT—Main Central thrust; LE—Lingshi exposure; STDS—South Tibetan detachment system; YCS—Yadong cross structure. (C) Geologic map of the Lingshi exposure. Mapping sources (see inset on right): 1—this study; 2—Gansser (1983); 3—Wu et al. (1998); 4—Kellett and Grujic (2012); 5—Grujic et al. (2011); 6—Long et al. (2011c). Inset on the right also shows stereoplots of stretching lineation and crenulation cleavage measurements (generated using Stereonet 8; Allmendinger et al., 2011). The STDS is simplified here at the Greater Himalayan–Chekha Formation contact; see Figures 2–4 for locations of the upper and lower limits of the STDS zone. undiff.—undifferentiated.

magnitude of isotherm telescoping across the full thickness of the STDS (Cottle et al., 2011; Law et al., 2011; Kellett and Grujic, 2012). In this study, we present data that illuminate trends in peak and deformation temperature, fabric development, finite strain, and kinematics along a transect through the STDS in northwestern Bhutan. These data facilitate definition of the boundaries and internal architecture of the STDS, allow estimation of offset magnitude, and are integrated with published geochronology to produce a detailed model of the structural evolution of the shear zone. We then use this case study to argue for the criteria that are most appropriate for definition of the boundaries of the STDS and other shear zones, and to demonstrate the utility of gradients in fabric intensity and finite strain when field criteria for delineating shear zone boundaries are not easily identifiable.

TECTONIC FRAMEWORK

Himalayan Geologic Background

The closure of the Neotethys Ocean culminated in collision of the Indian and Asian plates at ca. 50–55 Ma (e.g., Rowley, 1996; Leech et al., 2005; Najman et al., 2010). Following initial collision, deformation associated with continued India-Asia convergence has constructed the Himalayan-Tibetan orogen. South of the Indus-Tsangpo suture (Fig. 1A), rocks native to the Indian plate have been buried, metamorphosed, and stacked into a south-vergent thrust belt (e.g., Powell and Conaghan, 1973; LeFort, 1975; Mattauer, 1986). First-order structures in the thrust belt separate packages of rock with differing deformation histories and metamorphic grades. Immediately south of the suture, the TH package consists of low-grade to unmetamorphosed, Paleozoic–Mesozoic sedimentary rocks that were deposited on the southern Tethyan passive margin (e.g., Brookfield, 1993; Garzanti, 1999). To the south, the north-vergent, normal-sense STDS places TH rocks over high-grade (typically upper amphibolite-facies) metasedimentary and meta-igneous rocks of the GH package (Fig. 1A) (e.g., Burg, 1983; Herren, 1987; Burchfiel et al., 1992). GH rocks were buried to mid-crustal depths as early as the late Eocene–Oligocene (e.g., Hodges et al., 1996; Godin et al., 2001; Corrie and Kohn, 2011; Zeiger et al., 2015), and experienced partial melting and granite intrusion during the Miocene (e.g., Harrison et al., 1998). GH rocks overlie greenschist-facies metasedimentary rocks of the Lesser Himalayan package across the Main Central thrust, a major south-vergent shear zone that was active in the early Miocene (e.g., Gansser, 1964; Robinson et al., 2003; Kohn et al., 2004; Tobgay et al., 2012). The southern part of the orogen is defined by a brittle thrust belt that deforms Lesser Himalayan rocks into regional-scale duplex systems (e.g., Robinson et al., 2006; Long et al., 2011a; Webb, 2013). Near the modern deformation front, Miocene–Pliocene synorogenic rocks of the Subhimalayan package are involved in deformation (e.g., DeCelles et al., 1998; Ojha et al., 2000; Lavé and Avouac, 2000).

GH Rocks, TH Rocks, and the STDS in Northwestern Bhutan

The GH section in northwestern Bhutan consists of ~8 km of migmatitic, garnet- and sillimanite-bearing paragneiss, with interlayered schist, quartzite, and orthogneiss (Gansser, 1983; Kellett et al., 2009; Long et al., 2011c; Warren et al., 2011; Tobgay et al., 2012). On the basis of youngest detrital zircon peaks and crystallization ages of granite intrusions, deposition of GH sedimentary protoliths in Bhutan is bracketed between the Neoproterozoic and Ordovician (Long and McQuarrie, 2010; Tobgay et al., 2012; McQuarrie et al., 2013). Above the GH rocks, an ~50 km (E-W) by ~40 km (N-S) exposure of TH rocks, often referred to as the Lingshi klippe or syncline (e.g., Kellett and Grujic, 2012; Tobgay et al., 2012), is preserved (Fig. 1C). At its base, the lithologically heterogeneous Chekha

Formation is mapped as the lowest TH unit (e.g., Jangpangi, 1978; Gansser, 1983; Tangri and Pande, 1995; Grujic et al., 2002). In the western part of the Lingshi exposure, the Chekha Formation consists of biotite-garnet schist and calc-silicate gneiss, but marble is the dominant lithology in the eastern part (Gansser, 1983; Kellett and Grujic, 2012). In central Bhutan, deposition of the Chekha Formation is bracketed as Middle to Late Cambrian by ca. 515 Ma youngest detrital zircons (McQuarrie et al., 2013) combined with ca. 495 Ma trilobite fossils documented in overlying TH rocks (Hughes et al., 2011). Above the Chekha Formation, Paleozoic TH rocks in the Lingshi exposure include Cambrian and Carboniferous–Permian diamictite, quartzite, limestone, and slate (Gansser, 1983; Bhargava, 1995; Tangri and Pande, 1995). Higher in the section, Triassic–Jurassic and Cretaceous slate is exposed (Ganesan and Bose, 1982; Gansser, 1983).

At the Lingshi exposure, the STDS has been mapped as a north-vergent ductile shear zone that places the Chekha Formation over GH rocks (e.g., Grujic et al., 2002). Kellett et al. (2009) referred to this exposure, and to other STDS exposures mapped farther to the east in Bhutan, as the "outer STDS," to contrast them with the main exposure of the STDS that has been mapped along the Bhutan-Tibet border (the "inner STDS") (Fig. 1B) (Burchfiel et al., 1992; Edwards et al., 1996; 1999). Kellett et al. (2010) interpreted the outer STDS at the Lingshi exposure as a 2–3-km-thick high-strain zone defined by a dominantly top-to-north shear-sense, extending as much as ~1 km below and ~2 km above the GH-Chekha Formation contact.
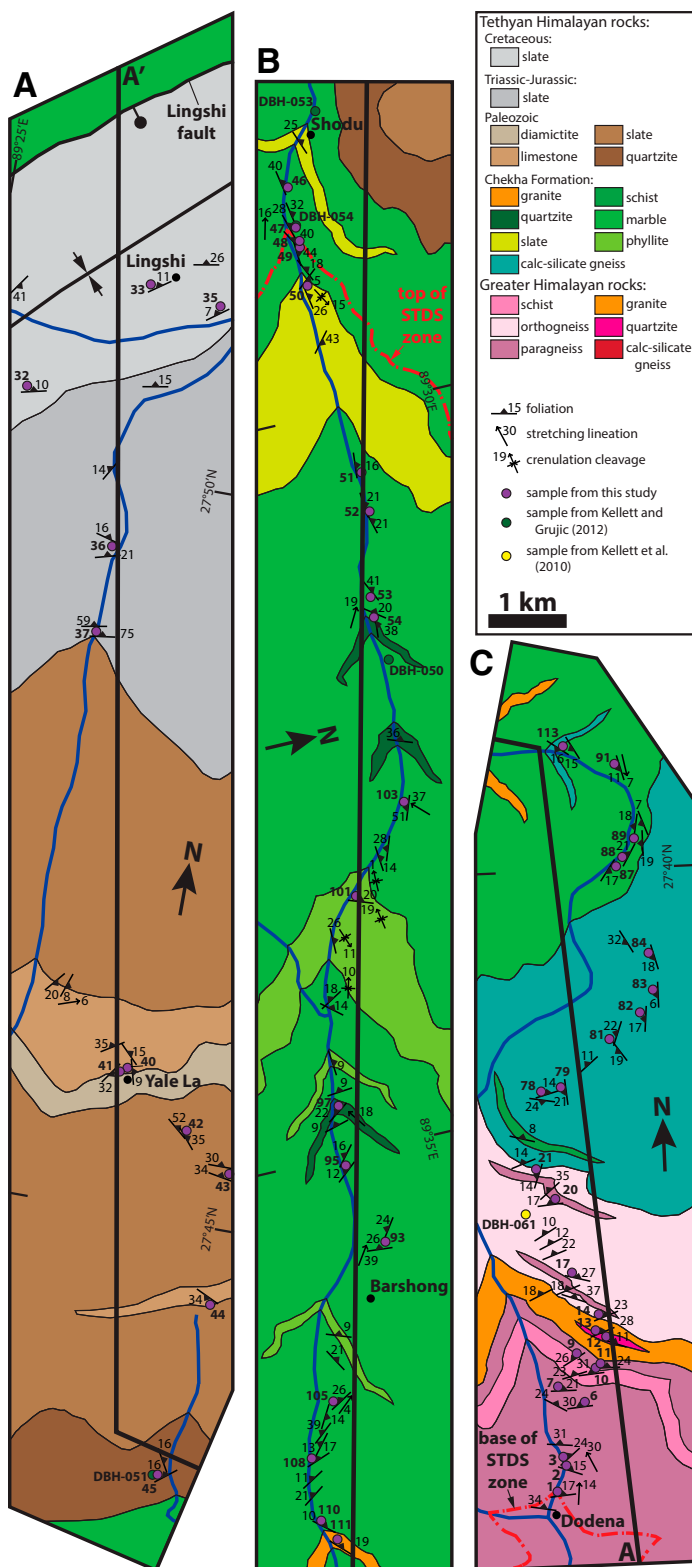
GH rocks collected within the STDS zone attained peak pressure-temperature conditions of ~6–9 kbar and ~620–790 °C (obtained using THERMOCALC; Kellett et al., 2010). Raman spectroscopy of carbonaceous material (RSCM) thermometry defines peak temperatures of ~300–450 °C at the top of the Chekha Formation, and ~200–300 °C for Paleozoic and Mesozoic TH rocks (Kellett and Grujic, 2012). GH rocks experienced prograde monazite growth between ca. 26 and 21 Ma (Kellett et al., 2010). Monazite inclusions within garnet that grew prior to STDS-related deformation cluster at ca. 23 Ma, which is interpreted as the timing of partial melting of GH rocks (Kellett et al., 2010). Partial melting and peak metamorphism were followed by north-vergent shearing on the STDS, accompanied by retrograde growth of high-Y monazite rims in GH rocks between ca. 19 and 15 Ma (Kellett et al., 2010) and crystallization of granite sills within the Chekha Formation as young as ca. 16.5 Ma (Kellett et al., 2009). ^{40}Ar/^{39}Ar muscovite thermochronology from Triassic–Jurassic TH rocks near Lingshi and from a granite sill in the Chekha Formation indicate cooling through ~425 °C at ca. 13–11 Ma (Kellett et al., 2009; Antolín et al., 2012).

On the northwestern margin of the Lingshi exposure, TH rocks are offset by the Lingshi fault (Fig. 1C), a SE-dipping brittle fault with normal and sinistral motion components (Gansser, 1983). The Lingshi fault has been correlated with the Yadong cross-structure, a series of NE-striking, active normal faults in southern Tibet (Fig. 1B) (Armijo et al., 1986; Wu et al., 1998). Motion on the Lingshi fault may have begun as early as ca. 14 Ma (Cooper et al., 2015).

TECTONOSTRATIGRAPHY OF THE DODENA-LINGSHI TRANSECT

In order to define trends in temperature, finite strain, and kinematics across the STDS in northwestern Bhutan, we mapped an ~50-km-long transect between the towns of Dodena and Lingshi (Figs. 1C and 2). A total of 141 outcrops were examined, with samples collected at 54 of these localities (see Data Repository Table DR1[1]). Rocks at all levels exhibit a

---

[1]GSA Data Repository Item 2019160, Tables DR1–DR3, Figures DR1–DR7, and Discussions DR1–DR6, is available at http://www.geosociety.org/datarepository /2019, or on request from editing@geosociety.org.

Figure 2. (A–C) Geologic strip maps of the Dodena-Lingshi transect (locations shown on Fig. 1C). The thick black line shows the location of the line of section for A–A'. STDS—South Tibetan detachment system.

dominant macroscopic foliation (Figs. 1 and 2), and mineral stretching lineations were observed in most outcrops and typically plunge shallowly NW (mean trend of 323°; Fig. 1C inset). Structural (i.e., foliation-normal) thicknesses were measured by projecting the apparent dip of foliation measurements onto a cross section (Fig. 3). Field stops and sample localities are projected onto a tectonostratigraphic column (Fig. 4), with structural distance listed relative to the base of the Chekha Formation. All structural distances in the following text are listed in meters below (negative numbers) or above (positive numbers) the base of the Chekha Formation. The transect encompasses a total thickness of 14,100 m, ranging from −3950 to +10,150 m. Lithologies and other features on the transect are described below from structurally low to high.

GH rocks: Between −3950 and −950 m below the base of the Chekha Formation, exposures are dominated by migmatitic (typically <5%–10% leucosomes by volume), sillimanite- and garnet-bearing paragneiss, which is interlayered with quartzite and schist. Between −950 and −650 m, deformed, foliation-parallel granite intrusions are interlayered with calc-silicate gneiss, quartzite, and paragneiss. Between −650 and 0 m, migmatitic orthogneiss with up to 30%–40% leucosomes by volume is dominant and is interlayered with migmatitic, sillimanite-garnet paragneiss. The structurally highest observed occurrence of sillimanite is at −25 m.

Chekha Formation (5550 m thick): We map the base of the Chekha Formation at an upward transition from orthogneiss to calc-silicate gneiss, which is similar to Gansser (1983) and Kellett and Grujic (2012). The basal 300 m of the Chekha Formation consists of calc-silicate gneiss interlayered with schist and quartzite. The structurally highest occurrence of leucosomes is at +75 m above the base of the Chekha Formation, and the structurally highest occurrence of garnet is at +250 m. The Chekha Formation is dominated by marble between +300 and +5550 m, with intervals of quartzite and phyllite between +1350 and +3200 m, and intervals of slate between +4000 and +5125 m. The structurally highest observed occurrences of biotite and muscovite porphyroblasts are at +1275 m and +4650 m, respectively.

Granite sills: Deformed granite sills are observed through the full examined thickness of GH rocks, and as high as +3200 m in the Chekha Formation (Fig. 4). However, they are most prevalent between −1800 and +800 m, where they locally account for up to 30%–40% of outcrops by volume (Figs. 5C, 5D). These sills typically range in thickness from ~0.1 to 2 m, have a solid-state foliation, and often exhibit boudinage (Fig. 5A, 5B).

Paleozoic TH rocks (2900 m thick): Following Gansser (1983), we map the contact between the Chekha Formation and overlying Paleozoic TH rocks at an upward transition from marble to quartzite and slate. Paleozoic TH rocks are observed between +5550 m and +8450 m, and are dominated by slate (note: structural thicknesses were measured normal to slaty cleavage, and not to sedimentary bedding, which is locally preserved in TH slates), with a 200-m-thick basal quartzite, limestone intervals at +5825–5875 m and +7075–7350 m, and diamictite at +6925–7075 m (Fig. 4).

Mesozoic TH rocks (>1700 m thick): Mesozoic TH rocks are mapped after Gansser (1983), and are dominated by gray to black, graphitic slate. They exhibit a minimum thickness of 1700 m, between +8450 and +10,150 m above the base of the Chekha Formation. Near Lingshi, the axis of a NE-trending open syncline, which can be traced for at least ~25 km (Fig. 1C), exposes the highest TH rocks on the transect.

Lingshi fault: The northern end of the transect crosses the NE-striking Lingshi fault, which places Cretaceous TH rocks in the hanging wall against Chekha Formation marble in the footwall. This relationship requires at least ~6 km of down-to-SE, normal-sense offset along the transect (Fig. 3). However, map relationships show that offset on the Lingshi fault decreases significantly along strike to the NE and SW (Gansser, 1983; Kellett and Grujic, 2012; this study).
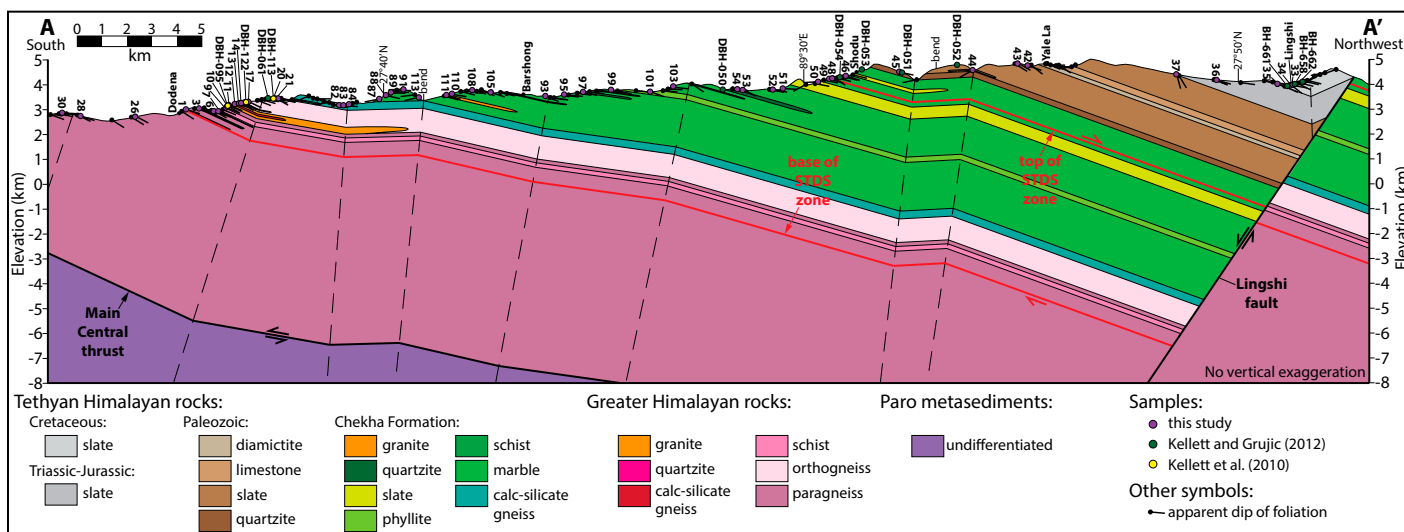
Figure 3. Cross section A–A′ along the Dodena-Lingshi transect (line of section shown on Fig. 1C). The thickness of Greater Himalayan rocks and the structural level of the Main Central thrust are supported by mapping to the south (Tobgay et al., 2010). STDS—South Tibetan detachment system.

STRUCTURAL OBSERVATIONS

Shear-Sense Indicators

Outcrop- and thin section-scale shear-sense indicators on the Dodena-Lingshi transect (Fig. 6) include C′-type shear bands, SC fabrics, mica fish, oblique foliations in recrystallized quartz, asymmetric folds, asymmetric boudinage, and leucosomes, granite sills, and rigid porphyroclasts sheared into σ-objects. Shear-sense indicators were observed within a total of 29 outcrops and 15 thin sections (Fig. 4). Though both top-to-SE and top-to-NW indicators are widely distributed through the transect, top-to-NW shear is dominant between −1825 and +775 m (Fig. 4). Additional shear-sense information demonstrated by quartz c-axis plots and stretching directions in finite strain analyses are shown on Figure 4, and are discussed below.

Quartz Recrystallization Microstructures

Dynamically recrystallized quartz was observed in thin sections of all GH samples and the lowest 2700 m of the Chekha Formation (Fig. 7). Here, we used the morphology of recrystallized quartz to interpret dominant recrystallization mechanisms and to estimate deformation temperature (e.g., Stipp et al., 2002; also see review in Law, 2014). We utilized the approximate deformation temperature ranges for quartz recrystallization mechanisms calibrated by Law (2014; his fig. 21) from Himalayan rocks in proximity to the Main Central thrust (Fig. 4) (as a caveat, differences in strain rate between the Main Central thrust and the STDS may also affect the apparent deformation temperature ranges, as recrystallization mechanisms are also sensitive to strain rate; e.g., Law, 2014). Four different recrystallization microstructures were observed: (1) chessboard extinction (CBE), characterized by extinction domains that intersect at approximately right angles within large (≥~0.25 mm) amoeboid quartz neoblasts (a neoblast is defined here as a visually distinct recrystallized grain) (Fig. 7A; e.g., Lister and Dornsiepen, 1982; Mainprice et al., 1986), which indicates deformation at ≥~630 °C (Stipp et al., 2002); (2) grain boundary migration (GBM), which is indicated by ~0.1–1.0 mm amoeboid quartz neoblasts (Fig. 7B; e.g., Guillope and Poirier, 1979; Urai

et al., 1986), and represents deformation at ~550–650 °C (Law, 2014); (3) subgrain rotation (SGR), which is defined by equigranular, polygonal, ~10–100 μm quartz neoblasts (Fig. 7C; e.g., Poirier and Nicolas, 1975; White, 1977; Guillope and Poirier, 1979), and indicates deformation at ~450–550 °C (Law, 2014); and (4) bulging (BLG), which is indicated by development of <~10 μm subgrains at quartz porphyroclast boundaries (a porphyroclast is defined here as a relict, detrital grain) (Fig. 7D; Bailey and Hirsch, 1962; Drury et al., 1985), and represents deformation at ~350–450 °C (Law, 2014).

On the Dodena-Lingshi transect, an overall pattern of recrystallization at progressively lower temperatures with increasing structural level is defined (Fig. 4). CBE was observed between −3950 and −1325 m (n = 5), GBM between −1825 and −25 m (n = 8), SGR between −1025 and +1975 m (n = 18), and BLG at +2700 m (n = 1). The average diameter of recrystallized quartz grains was measured for seven quartz-rich samples (see Fig. DR7 [footnote 1] for a graph of grain size versus structural height), which are distributed between −1550 and +150 m. Samples dominated by SGR recrystallization yielded diameters between ~40 and ~100 μm, and those dominated by GBM recrystallization yielded diameters between ~100 and ~230 μm. However, these data did not yield a consistent pattern of grain size with structural height.

RSCM THERMOMETRY

Carbonaceous material was analyzed from thin sections of GH metasedimentary rocks (n = 4), the Chekha Formation (n = 14), and Paleozoic-Mesozoic TH rocks (n = 3), in order to calculate peak metamorphic temperatures using the RSCM thermometer (e.g., Beyssac et al., 2002, 2003; Rahl et al., 2005). Measurements were made at Arizona State University, Tempe, Arizona, USA (see Data Repository [footnote 1] for analytical methods and supporting data). Carbonaceous material was typically present as ~5–25 μm patches (Figs. 8A–8C), and sometimes as laminations (Fig. 8D). Examples of representative Raman spectra for each sample are shown on Figure 8E. We followed the analytical methods of Rahl et al. (2005), in which the RSCM thermometer for rocks that achieved peak temperatures between ~100 and 740 °C was determined by measuring the height ratio (R1) and area ratio (R2) of four first-order
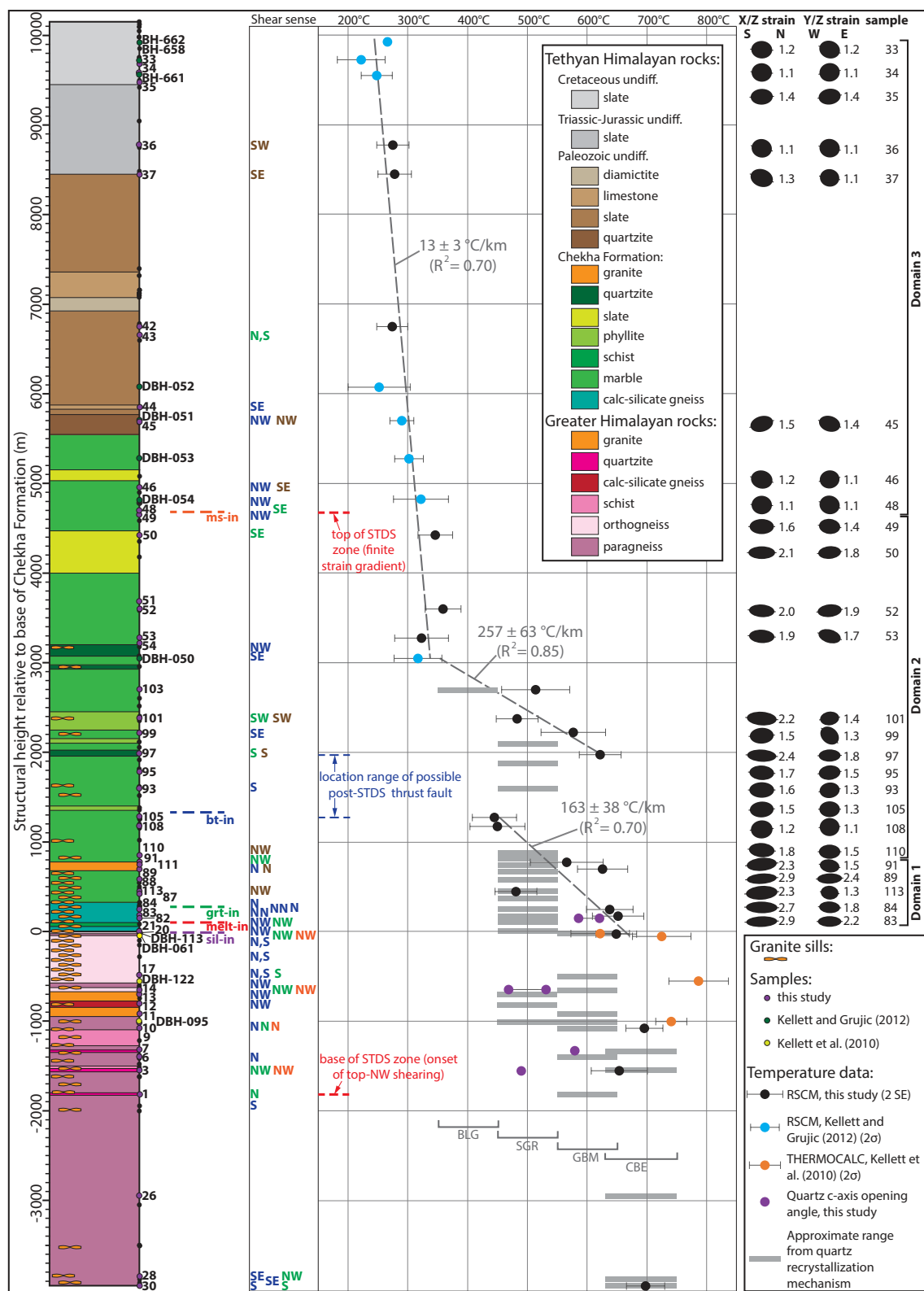
Figure 4. Tectonostratigraphic column of the Dodena-Lingshi transect (calculated from structural thicknesses on Fig. 3), showing samples, mineral isograds (abbreviations after Whitney and Evans, 2010), shear-sense indicators (data shown in green were observed in thin section, blue were observed in outcrop, orange were observed in quartz *c*-axis plots, and brown were defined by the elongation direction of quartz porphyroclasts), peak and deformation temperature data, and finite strain data versus structural height relative to the base of the Chekha Formation. RSCM—Raman spectroscopy of carbonaceous material; STDS—South Tibetan detachment system; undiff.—undifferentiated. Abbreviations for quartz recrystallization microstructures: BLG—grain boundary bulging; SGR—subgrain rotation; GBM—grain boundary migration; CBE—chessboard extinction.
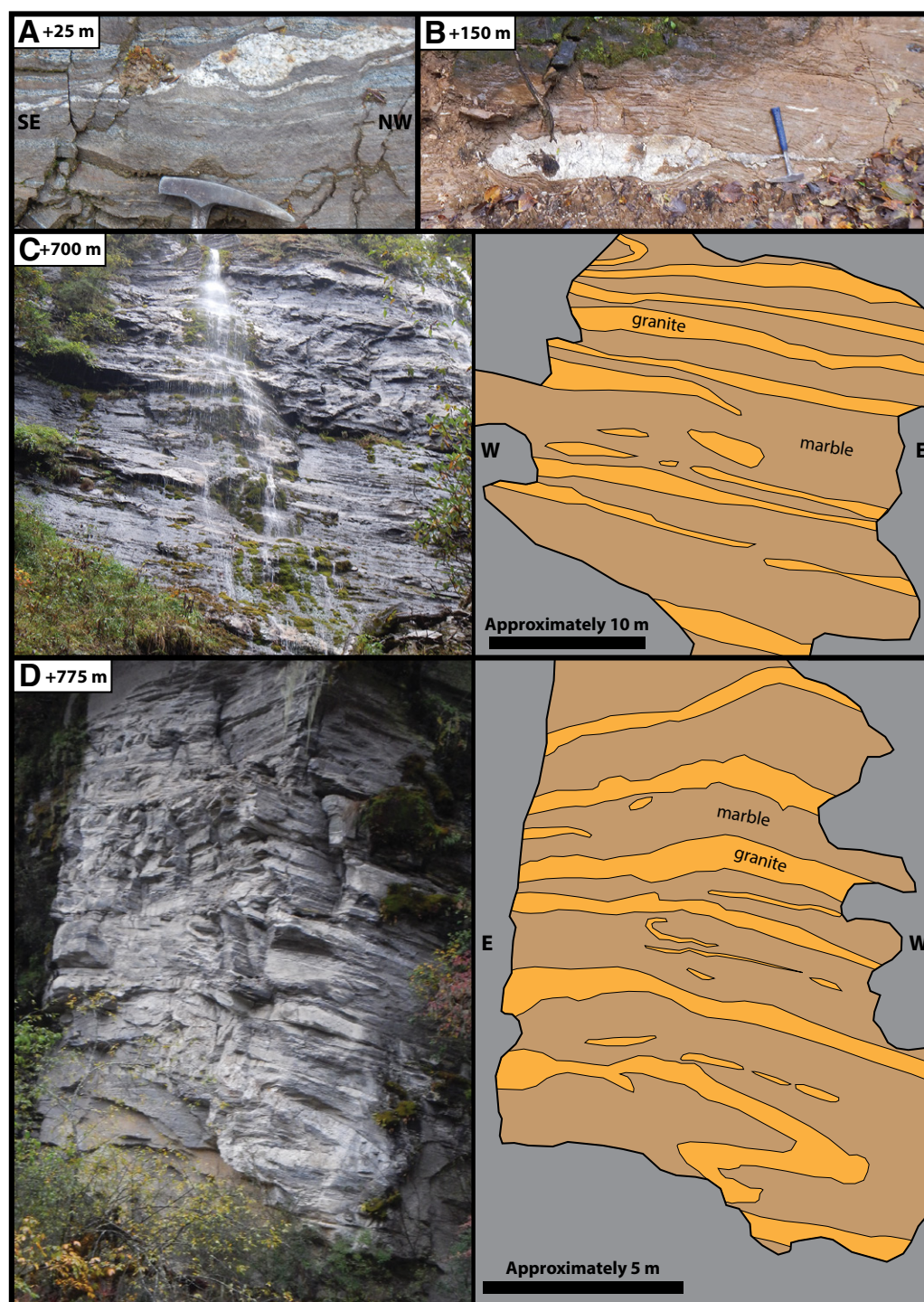
Figure 5. Photographs of deformed granite sills intruding the Chekha Formation within the South Tibetan detachment system (stop numbers are referenced to Figs. 2–4). (A) Top-to-NW, boudinaged, ~10-cm-thick sill within calc-silicate gneiss (stop 22). (B) Boudinaged, ~20-cm-thick sill within marble (stop 81). (C, D) Marble cliffs intruded by m-scale deformed sills (C—stop 89; D—stop 91), with annotations shown on the right.
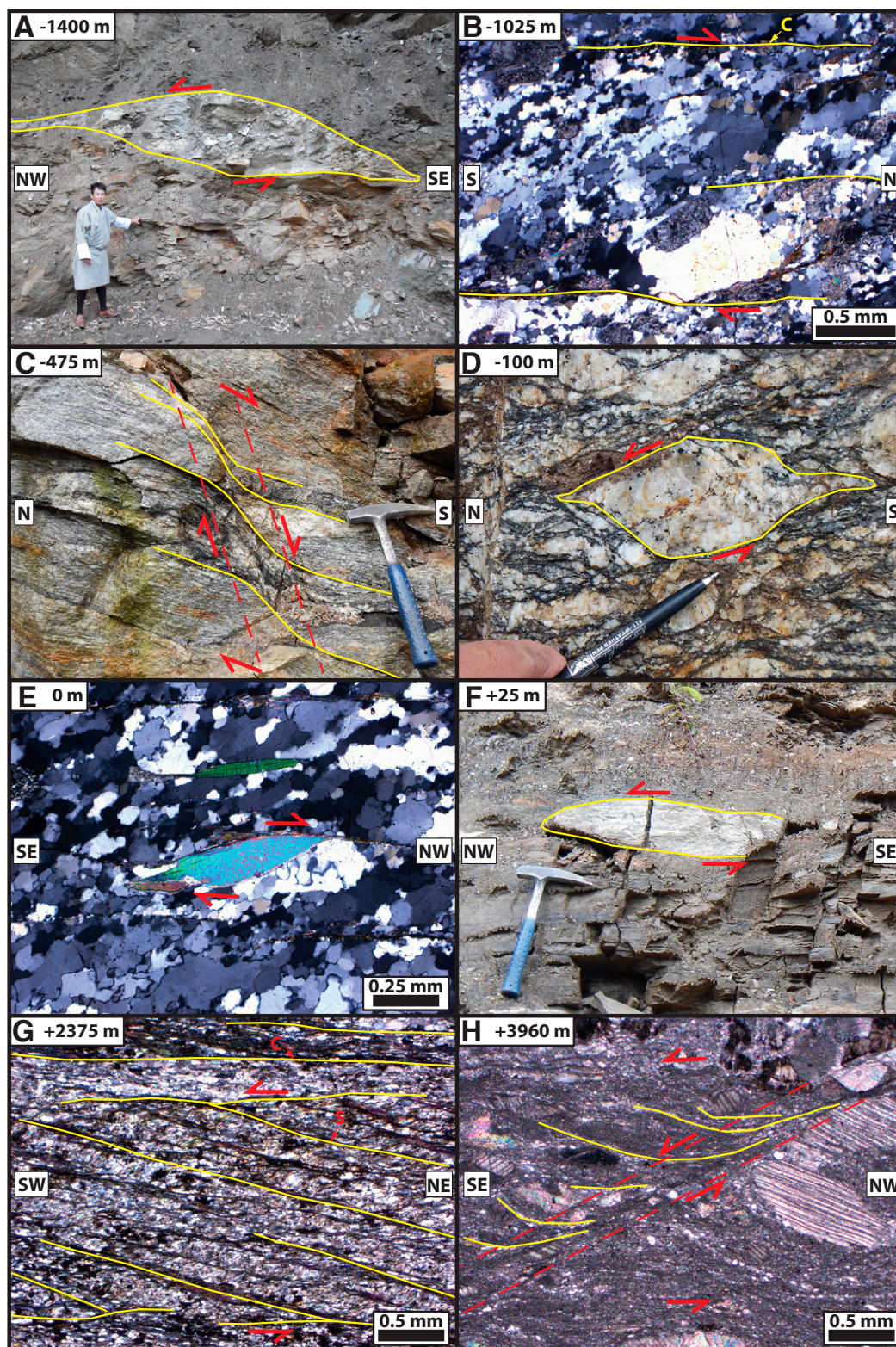
Figure 6. Photographs and photomicrographs (taken in cross-polarized light) illustrating representative shear-sense indicators observed on the Dodena-Lingshi transect (organized from structurally low to high; stop numbers referenced to Figs. 2–4). (A) Granite sill sheared into a top-to-NW σ-object (stop 6). (B) Oblique foliation in recrystallized quartz, defining a top-to-N shear-sense (stop 10). (C) Top-down-to-S C′-type shear band, defining an overall top-to-S shear sense (stop 17). (D) Feldspar augen sheared into a top-to-N σ-object (stop 19). (E) Top-to-NW mica fish within recrystallized quartz that also exhibits a top-to-NW oblique foliation (stop 21A). (F) Boudinaged granite sill sheared into a top-to-NW σ-object (stop 22). (G) Top-to-SW SC fabric (stop 101). (H) Top-down-to-SE C′-type shear band, which defines an overall top-to-SE shear-sense (stop 48).

Figure 7. Cross-polarized light photomicrographs illustrating representative quartz recrystallization microstructures. (Sample numbers are referenced to Figs. 2–4.) (A) Chessboard extinction (CBE) microstructure, characterized by ≥0.25 mm quartz neoblasts with multiple extinction domains with boundaries that intersect at approximately right angles (red arrow). (B) Grain boundary migration (GBM) microstructure, characterized by ~0.25–1.0 mm, cuspate, interfingering, "amoeboid" quartz neoblasts. (C) Subgrain rotation (SGR) microstructure, defined by equigranular, ~10–50 μm quartz neoblasts. (D) Bulging (BLG) recrystallization localized along boundaries between adjacent quartz porphyroclasts (red arrows).

A CBE, sample 26, -2950 m

0.25 mm

B GBM, sample 14, -650 m

0.50 mm

C SGR, sample 10, -1025 m

0.25 mm

D BLG, sample 103, +2700 m

0.25 mm

Raman peaks (G, D1, D2, D3) in the relative wavenumber range of 1200–1800 cm^{-1}. Mean peak temperatures of multiple measurements (varying between 9 and 16 for individual samples) are shown on Table 1, and are reported at a 2 standard error (SE) level, which takes into account internal uncertainty and the external uncertainty from the Rahl et al. (2005) calibration (e.g., Cooper et al., 2013; Long et al., 2016, 2017).

Four GH samples, which span structural heights between −3950 and −25 m, yielded overlapping temperatures between ~650 and 700 °C (Fig. 4). The lowest seven Chekha Formation samples define an overall upward decrease from ~650 to ~450 °C between +175 and +1275 m. Above this, four Chekha Formation samples between +1975 and +2700 m define an abrupt increase to ~620 °C, followed by an upward decrease to ~480–510 °C. Moving structurally upward, three Chekha Formation samples between +3275 and +4425 m overlap between ~320 and 360 °C, and three TH samples between +6750 and +8775 m overlap between ~270 and 280 °C.

The 21 new RSCM temperatures from this study were combined with published peak temperatures from 12 samples from the Dodena-Lingshi transect and proximal areas (Table 2; Fig. 4). These include THERMO-CALC temperatures determined from four GH samples (Kellett et al., 2010), which yielded temperatures of ~740–790 °C between −1000 and −50 m, and ~620 °C at −20 m. In addition, Kellett and Grujic (2012) presented RSCM temperatures from three Chekha Formation samples (+3050–5275 m), which yielded temperatures of ~300–320 °C, two Paleozoic TH samples (+5700, +6075 m), which ranged from ~250 to 290 °C, and three Mesozoic TH samples (+9550–9925 m), which ranged from ~220 to 270 °C.

Combining the new and published temperature data sets yielded the following trends: Between −3950 and −50 m, peak temperatures are between ~650 and 750 °C (n = 5), with one outlier of ~790 °C (Fig. 4). Between −50 and +1275 m, temperatures decrease upward from ~625 to 725 °C to ~450 °C (n = 9, with one outlier (sample 113 at +450 m) that falls below this trend), which is best-fit by a telescoped, upright thermal field gradient of 163 ± 38 °C/km (R^2 = 0.70). There is a data gap between samples at +1275 and +1975 m, across which temperatures increase upward from ~450 to ~620 °C. Above this, between +1975 and +3050 m, temperatures again decrease upward from ~620 to ~320 °C (n = 5), which is best-fit by a steep, upright field gradient of 257 ± 63 °C/km (R^2 = 0.85). Above this, between +3050 and +9925 m, temperatures gradually decrease upward from ~320–360 °C to ~220–265 °C (n = 14), which is best-fit by a gentle, upright field gradient of 13 ± 3 °C/km (R^2 = 0.70).

QUARTZ CRYSTALLOGRAPHIC FABRICS

In order to provide information on shear-sense, the 3-D strain field, deformation temperature, and kinematic vorticity (e.g., Lister and Hobbs, 1980; Schmid and Casey, 1986; Wallis, 1992, 1995; Kruhl, 1998; Morgan and Law, 2004), the orientations of quartz c-axes were measured in seven quartzite samples collected from structural levels between −1550 and +150 m (Table 3; Fig. 9). Quartz c-axis orientations were measured on foliation-normal, lineation-parallel thin sections using an automated
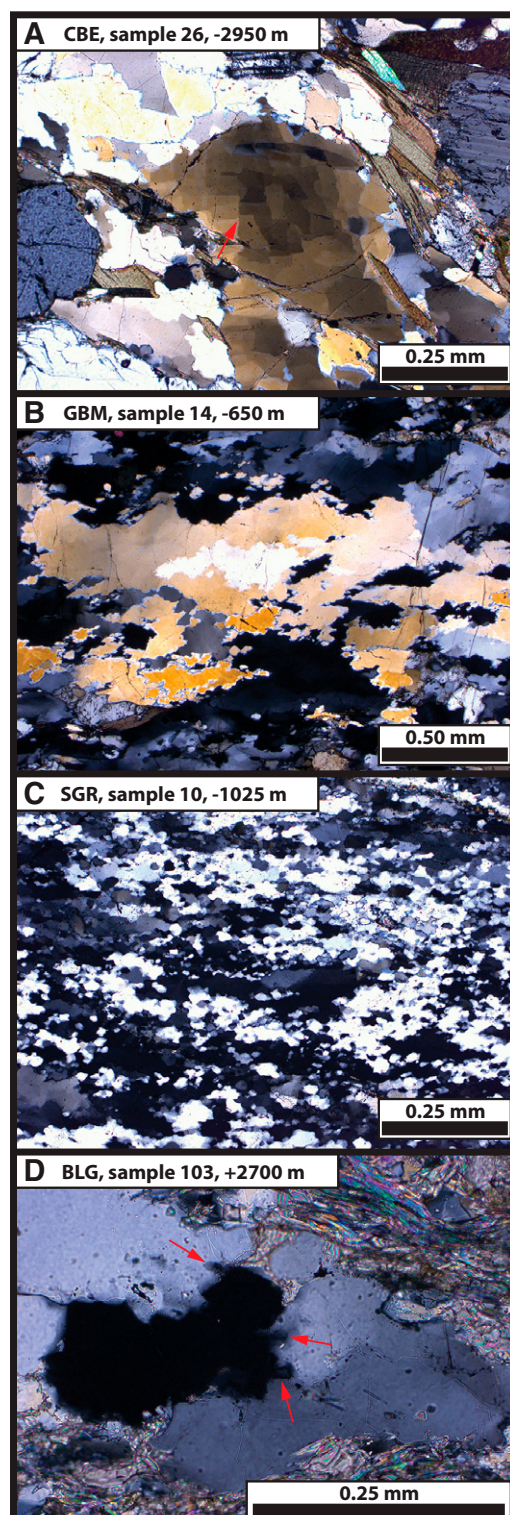
crystal fabric analyzer (e.g., Wilson et al., 2009; Peternell et al., 2011; Larson et al., 2013; Larson and Cottle, 2014) (see Data Repository for details on analytical methods). The c-axis measurements are plotted on lower-hemisphere, equal-area stereonets in Figure 9.

All samples exhibit crystallographic preferred-orientations (CPO) characteristic of recrystallization at <~650 °C (e.g., Lister and Hobbs, 1980;
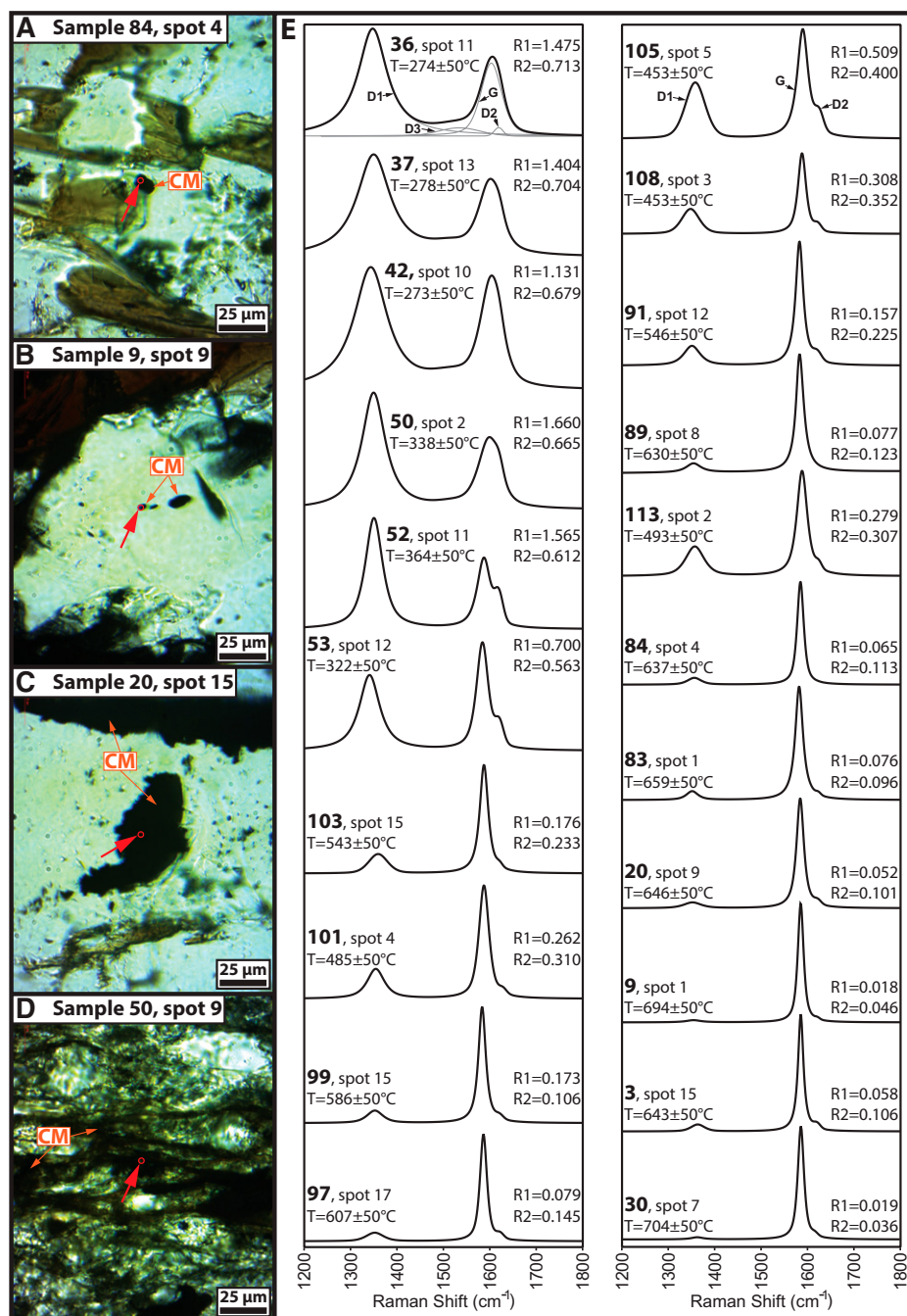
Figure 8. (A–D): Photomicrographs (plane-polarized light) of representative examples of analyzed carbonaceous material (CM), which typically occurs as isolated ~5–25 μm diameter patches (A–C) or laminations (D). The red arrow in each photo points to the probed area. (Sample numbers are referenced to Figs. 2–4.) (E) Examples of representative Raman spectra from single spot analyses of each sample, in order of increasing structural height. Positions of the graphite band (G) and defect bands (D1, D2, D3) are labeled on the top spectrum in each column. Peak temperatures (T) and R1 and R2 parameters are calculated after Rahl et al. (2005). Single spot analyses are listed here with errors of ±50 °C, which is the external uncertainty from the Rahl et al. (2005) calibration.

TABLE 1. SUMMARY OF RSCM PEAK TEMPERATURES FROM DODENA-LINGSHI TRANSECT SAMPLES

Sample	Map unit	Lithology	Structural height (m)	R1		R2		Peak temperature (°C)			
				Mean	1σ	Mean	1σ	Mean	1σ	2 SE	n
36	THMzu	Graphitic slate	8775	1.428	0.079	0.708	0.014	275	17	27	15
37	THMzu	Graphitic slate	8450	1.426	0.108	0.704	0.013	278	16	28	14
42	THPzu	Graphitic slate	6750	1.266	0.136	0.693	0.013	274	12	26	15
50	THck	Phyllite	4425	1.728	0.302	0.654	0.029	346	25	29	15
52	THck	Marble	3600	1.249	0.297	0.606	0.032	359	33	30	16
53	THck	Marble	3275	1.020	0.351	0.607	0.102	323	75	45	16
103	THck	Marble	2700	0.305	0.249	0.289	0.132	514	80	57	11
101	THck	Calcareous phyllite	2375	0.319	0.128	0.326	0.077	483	50	35	16
99	THck	Marble	2225	0.085	0.045	0.175	0.089	577	83	54	13
97	THck	Phyllitic quartzite	1975	0.068	0.038	0.128	0.057	622	50	35	16
105	THck	Marble	1275	0.511	0.055	0.407	0.029	445	22	37	9
108	THck	Marble	1175	0.375	0.189	0.368	0.099	450	74	46	15
91	THck	Schist	775	0.156	0.148	0.204	0.142	566	110	61	16
89	THck	Calcareous quartzite	700	0.054	0.041	0.120	0.068	626	61	42	14
113	THck	Calc-silicate gneiss	450	0.318	0.117	0.327	0.068	481	45	35	15
84	THck	Schist	250	0.056	0.028	0.109	0.051	638	46	39	12
83	THck	Calc-silicate gneiss	175	0.067	0.060	0.100	0.072	652	60	43	13
20	GH	Schist	–25	0.057	0.030	0.099	0.046	649	40	34	14
9	GH	Schist	–1075	0.021	0.018	0.045	0.034	696	31	31	14
3	GH	Quartzite	–1550	0.059	0.044	0.096	0.059	654	50	47	9
30	GH	Paragneiss	–3950	0.023	0.023	0.043	0.040	698	36	32	15

Note: R1, R2, and peak temperature values calculated using the calibration of Rahl et al. (2005). Internal variability in R1, R2, and peak temperature is indicated by 1σ uncertainty. Temperature is also reported with 2 standard errors (SE), calculated after Cooper et al. (2013), from quadratic addition of 1σ internal error and external error of ±50 °C from the Rahl et al. (2005) calibration, divided by the square root of the number of analyses (n). GPS locations of all samples are shown on Table DR1 in the Data Repository (see text footnote 1). RSCM—Raman spectroscopy of carbonaceous material. Map units: THMzu—Mesozoic Tethyan Himalayan rocks; THPzu—Paleozoic Tethyan Himalayan rocks; THck—Chekha Formation; GH—Greater Himalayan rocks.

Behrmann and Platt, 1982; Bouchez et al., 1983). Samples 3 and 14 yielded weak type I crossed-girdle patterns and sample 82 exhibits a type II crossed-girdle pattern, which indicate that basal <a>, rhomb <a>, and prism <a> slip systems were active (e.g., Lister, 1977; Schmid and Casey, 1986). Sample 7 yielded a poorly developed crossed-girdle pattern, but its type (I or II) could not be visually determined. Samples 10 and 21A exhibit single-girdle patterns, which result from prism <a> and rhomb <a> dominant slip (e.g., Lister and Hobbs, 1980; Schmid and Casey, 1986). Sample 13 yielded a center point maxima, indicating prism <a> dominant slip (e.g., Mainprice et al., 1986; Passchier and Trouw, 2006). The fabric patterns from these seven samples are indicative of deformation within a 3-D strain field that approximates plane strain (e.g., Schmid and Casey, 1986).

Statistical parameters can be used to quantify the intensity (i.e., non-randomness) of fabric development, and have recently been applied as strain magnitude proxies to characterize strain patterns across Himalayan shear zones (Larson et al., 2017; Starnes et al., 2017). Here, we utilize the cylindricity index (B) of Vollmer (1990), which is based on eigenvector analysis of *c*-axis directions (e.g., Woodcock, 1977; Mainprice et al., 2014). Vollmer (1990) divided quartz fabrics into three end-member components: point (P), girdle (G), and random (R), where P + G + R = 1. The formation of a strong P or G fabric depends upon the active slip system during quartz recrystallization (Barth et al., 2010), and B is defined as the sum of the P and G values. B is a measure of the non-randomness of a fabric, where 0 represents a completely random fabric and 1 represents a completely non-random fabric. P, G, R, and B values (Table 3) were calculated from the quartz *c*-axis measurements using the program Orient (Vollmer, 2017 [Orient 3: Spherical projection and orientation data analysis program, www.frederickvollmer.com]) (see Fig. DR6 [footnote 1] for a ternary plot of P, G, and R values). B values on the Dodena-Lingshi transect (Fig. 9D) are low (0.21; sample 3) at −1550 m, increase to values between 0.48 and 0.87 between −1325 and 0 m (samples 7, 10, 13, 14, 21A), and decrease to 0.10 at +150 m (sample 82).

Assuming a consistent, critically resolved shear stress, negligible hydrolytic weakening, and an invariant strain rate, the opening angle exhibited in crossed-girdle quartz *c*-axis fabrics may be related to the temperature at which the fabrics were "locked in" during the final stages of dynamic recrystallization (e.g., Kruhl, 1998; Morgan and Law, 2004; Faleiros et al., 2016). Here, we use the pressure-independent calibration of Faleiros et al. (2016) to estimate opening angle deformation temperatures from four samples that yielded crossed-girdle fabrics. The samples exhibited a total range of opening angles between 61° and 83° (Fig. 9; Table 3), which correspond to deformation temperatures of 490 °C (sample 3), 579 °C (sample 7), 469–531 °C (sample 14), and 586–621 °C (sample 82).

Four samples exhibit asymmetric *c*-axis fabrics, which allow for interpretation of shear-sense. The central part of the fabric skeletons for samples 3, 10, 14, and 21A are inclined to the NW relative to foliation, defining a top-to-NW shear sense (Fig. 9B). This is consistent with top-to-NW microstructural shear-sense indicators observed in thin sections of all four samples.

Using the quartz shape-preferred orientation method of Wallis (1992, 1995), the angle between foliation and the line normal to the central girdle segment of a quartz *c*-axis fabric (β) can be combined with the mean elongation angle of recrystallized quartz neoblasts measured relative to foliation (θ'_{ISA1}) to calculate the mean kinematic vorticity number (W_m). W_m is a ratio that quantifies the relative contributions of pure shear and simple shear (e.g., Means et al., 1980; Passchier, 1987; Tikoff and Fossen, 1993; Means, 1994); a value of 0 represents entirely pure shear, 1 represents entirely simple shear, and equal contributions occur at 0.71 (e.g., Law et al., 2004). Here, we assume the simplified case of steady-state plane strain for estimation of W_m (e.g., Fossen and Tikoff, 1993; Johnson et al., 2009), which is supported by fabric patterns indicative of approximate plane strain conditions observed between −1550 and +150 m. β and θ'_{ISA1} angles were measured for GH samples 3, 10, 14, and 21A (Fig. 9; Table 3; see Data Repository [footnote 1] for supporting data), which yielded W_m

TABLE 2. PUBLISHED *P-T* AND RSCM DATA FROM THE DODENA-LINGSHI TRANSECT AND PROXIMAL AREAS

Sample	Map unit	Lithology	Structural height (m)	T (°C) (±2σ)	P (kbar) (±2σ)	Technique	Location relative to transect	Data source
BH-662	THMzu	Slate	9925	266 ± 4	–	RSCM	2 km to east	Kellett and Grujic (2012)
BH-658	THMzu	Slate	9725	222 ± 40	–	RSCM	2 km to west	Kellett and Grujic (2012)
BH-661	THMzu	Slate	9550	248 ± 26	–	RSCM	2 km to east	Kellett and Grujic (2012)
DBH-052	THPzu	Slate	6075	252 ± 52	–	RSCM	along transect	Kellett and Grujic (2012)
DBH-051	THPzu	Quartzite	5700	290 ± 20	–	RSCM	along transect	Kellett and Grujic (2012)
DBH-053	THck	Marble	5275	302 ± 24	–	RSCM	along transect	Kellett and Grujic (2012)
DBH-054	THck	Marble	4825	322 ± 46	–	RSCM	along transect	Kellett and Grujic (2012)
DBH-050	THck	Marble	3050	317 ± 40	–	RSCM	along transect	Kellett and Grujic (2012)
DBH-113	GH	Paragneiss	–20	622 ± 49	–	THERMOCALC	13 km to west	Kellett et al. (2010)
DBH-061	GH	Paragneiss	–50	725 ± 49	6.2 ± 1.7	THERMOCALC	along transect	Kellett et al. (2010)
DBH-122	GH	Paragneiss	–550	787 ± 50	6.9 ± 1.5	THERMOCALC	14 km to west	Kellett et al. (2010)
DBH-095	GH	Paragneiss	–1000	741 ± 26	9.0 ± 0.8	THERMOCALC	15 km to west	Kellett et al. (2010)

Note: GPS locations for these samples are available in Kellett and Grujic (2012) and Kellet et al. (2010). RSCM—Raman spectroscopy of carbonaceous material. Map units: THMzu—Mesozoic Tethyan Himalayan rocks; THPzu—Paleozoic Tethyan Himalayan rocks; THck—Chekha Formation; GH—Greater Himalayan rocks.

TABLE 3. SUMMARY OF PARAMETERS FOR DETERMINATION OF DEFORMATION TEMPERATURE AND KINEMATIC VORTICITY FROM QUARTZ *C*-AXIS FABRIC DATA FROM SAMPLES ON THE DODENA-LINGSHI TRANSECT

Sample	Unit	Lithology	Height above base of Chekha Formation (m)	Quartz recrystallization mechanism	Average recrystallized grain diameter (μm) (±1 SD)	Quartz c-axis opening angle	Opening angle deformation temp. (°C)[1]	β (°)	θ'$_{ISA1}$ (±1 SE)	W$_m$ range from quartz SPO method[2]	% Simple shear from quartz SPO method[3]	Quartz c-axis fabric components			Cylindricity Index (B)
												P	G	R	
82	THck	quartzite	150	SGR	61 ± 31	78°, 83°	586-621 ± 50	1°	–2 ± 2°	0.03–0.17	5–15%	0.09	0.01	0.90	0.10
21A	GH	quartzite	0	SGR	87 ± 62	–	–	–13°	–13 ± 2°	0.74–0.83	55–65%	0.48	0.39	0.13	0.87
14	GH	quartzite	–650	GBM	144 ± 116	61°, 70°	469-531 ± 50	–9°	–9 ± 2°	0.53–0.64	35–45%	0.34	0.15	0.51	0.49
13	GH	quartzite	–700	SGR	100 ± 57	–	–	–	–	–	–	0.59	0.02	0.38	0.62
10	GH	quartzite	–1025	SGR	43 ± 33	–	–	–13°	–16 ± 2°	0.81–0.88	60–70%	0.48	0.26	0.26	0.74
7	GH	quartzite	–1325	CBE	227 ± 154	77°	579 ± 50	–	–	–	–	0.35	0.13	0.52	0.48
3	GH	quartzite	–1550	CBE	105 ± 80	64°	490 ± 50	–18°	–8 ± 2°	0.74–0.83	55–65%	0.07	0.13	0.79	0.21

Note: β—acute angle between foliation and line normal to central axis of single or crossed girdle in quartz c-axis plot (after Law et al., 2013); θ'$_{ISA1}$—acute angle between foliation and mean angle of long axes of quartz neoblasts (after Johnson et al., 2009); W$_m$—mean kinematic vorticity number for plane strain deformation; SD—standard deviation; SE—standard error; SPO—shape-preferred orientation; P—Point fabric component; G—girdle fabric component; R—random fabric component; B—cylindricity index (Vollmer, 1990); THck—Chekha Formation; GH—Greater Himalayan rocks; SGR—subgrain rotation; GBM—grain boundary migration; CBE—chessboard extinction. GPS locations of all samples are shown on Table DR1 (see text footnote 1).
[1]Opening angle temperatures (temp.) calculated from Faleiros et al. (2016). Temperatures are reported with ±50 °C error (Kruhl, 1998).
[2]Calculated using the equation W$_m$ = sin(2*(β+θ'$_{ISA1}$)), from Wallis (1992, 1995).
[3]Percent simple shear values were determined from Law et al. (2004), and are rounded to the nearest 5%.
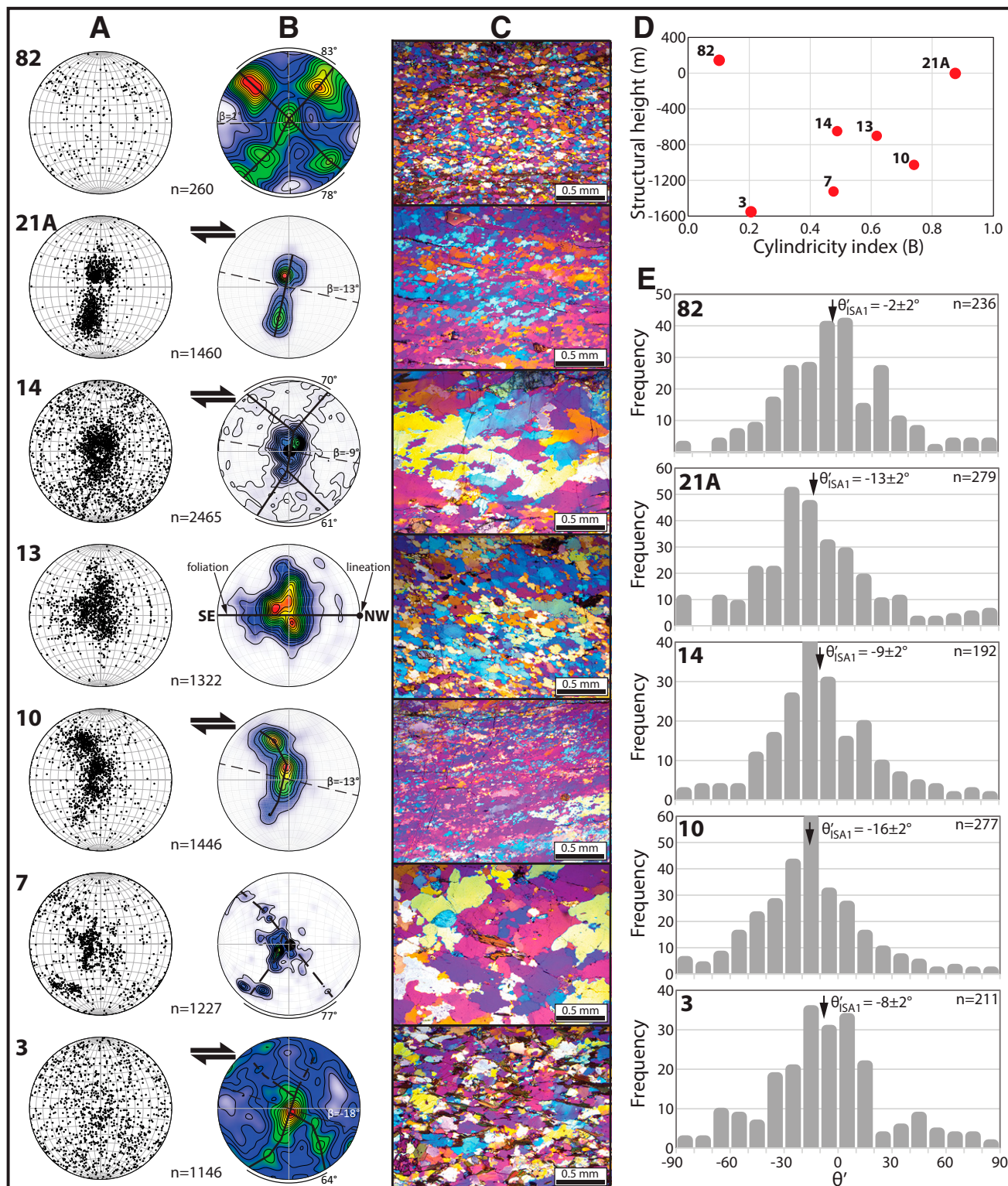
Figure 9. (A, B) Quartz *c*-axis orientations plotted as equal area stereographic projections (created using Orient 3.7.1; Vollmer, 2017). Plots are ordered in ascending structural position, and are oriented with foliation as a vertical plane and lineation as a horizontal line (see example shown for sample 13), with the view direction toward the SW. Column A shows stereoplots of individual *c*-axes, and column B shows *c*-axis pole figures (contoured relative to multiples of a random distribution), with visually interpreted fabric skeletons (e.g., Lister and Williams, 1979) drawn. The number of axes measured (n) are shown, as well as β angles, fabric opening angles, and interpreted shear-sense. Column C shows photomicrographs of each sample (XPL), taken with a 540 nm λ plate inserted. D shows a graph of cylindricity index versus structural height. E shows frequency histograms (with 10° bins) of θ′ measurements (the angle between the long axis of recrystallized quartz neoblasts and foliation; e.g., Ramsay and Huber, 1983), which were used to determine the θ'_{ISA1} angle.

ranges of 0.74–0.83, 0.81–0.88, 0.53–0.64, and 0.74–0.83, respectively. This corresponds to a range of 55%–70% simple shear, with one outlier of 35%–45% (sample 14). β and θ'_{ISA1} angles were measured for Chekha Formation sample 82, which yielded a W_m range of 0.03–0.17 (5%–15% simple shear, 85%–95% pure shear).

FINITE STRAIN DATA

All GH samples exhibit complete recrystallization of quartz (e.g., Fig. 7). However, between +175 and +2700 m, several Chekha Formation samples contain non-recrystallized, elongated quartz porphyroclasts that are isolated within a mica- or calcite-rich matrix (Fig. 10A), and quartz within all Chekha Formation and TH samples above +2700 m is not recrystallized (Fig. 10B). We investigated the magnitude and orientation of 3-D finite strain in 19 Chekha Formation samples and 6 TH samples distributed between +175 and +9675 m by performing the Rf-ϕ method (e.g., Ramsay, 1967; Dunnet, 1969) on elongated, non-recrystallized quartz porphyroclasts (supporting data in the Data Repository). Two foliation-normal thin sections were cut from each sample, one parallel (denoted with "A") and one normal (denoted with "B") to stretching lineation, which are interpreted to approximate the XZ and YZ strain planes, respectively. 2-D strain ellipses from each thin section are plotted on Figure 4, and strain data are summarized in Table 4. For all samples, the 2-D strain ratio (Rs) in the "A" thin section was either greater than or equivalent within error to Rs in the "B" thin section, which supports the use of foliation and lineation to approximate the principal strain directions. In addition, the quartz c-axis fabrics on Figure 9, by analogy with experiments and numerical modeling of fabric development, also demonstrate that stretching lineation in the analyzed samples is parallel to the maximum finite stretch (X) direction (e.g., Lister et al., 1978; Lister and Hobbs, 1980).

Competency contrasts between matrix and clasts can result in heterogeneous strain partitioning (e.g., Sanderson, 1982; Holyoke and Tullis, 2006), and quartz clasts often exhibit lower elongation magnitudes than the surrounding mica-rich matrix (e.g., Tullis and Wenk, 1994; Treagus and Treagus, 2002; Yonkee et al., 2013). Therefore, we interpret that our strain magnitudes likely represent minimum values.

Our data show an overall decrease in strain magnitude with increasing structural level (Fig. 4), and can be divided into three vertical domains: (1) the lowest 5 Chekha Formation samples (+175 to +775 m), which yielded average $Rs_{[X/Z]}$ and $Rs_{[Y/Z]}$ ratios of 2.60 ± 0.10 (errors at 1 SE level) and 1.85 ± 0.20, respectively; (2) Chekha Formation samples between +850 and +4650 m (n = 12), which yielded average $Rs_{[X/Z]}$ and $Rs_{[Y/Z]}$ ratios of 1.80 ± 0.10 and 1.50 ± 0.05; and (3) Chekha Formation and TH samples between +4700 and +9675 m (n = 8), which yielded average $Rs_{[X/Z]}$ and $Rs_{[Y/Z]}$ ratios of 1.25 ± 0.05 and 1.20 ± 0.05.

On a Flinn diagram (Fig. 10C), most ellipsoids plot entirely in the flattening field (n = 15), with nine samples that exhibit uncertainty ranges that overlap the plane strain line, and one sample that plots entirely in the constrictional field. ϕ angles were measured relative to foliation and are therefore equivalent to the parameter θ′ of Ramsay and Huber (1983) (from this point on ϕ is referred to as θ′; see discussion DR5 (see footnote 1) for additional details on the orientation relationship between macroscopic foliation and shear direction). The sign convention used for θ′ is positive if the grain long axis is inclined toward the NW or NE relative to foliation, and negative if inclined toward the SE or SW. Thirty-nine of the 50 thin sections yielded θ′ values between ±10°. The remaining 11 thin sections yielded values between ±11–19°, with one outlying value of +42°. The Flinn diagram results and low θ′ values together indicate that most samples underwent layer-normal flattening strain, with some approaching plane strain conditions.

We estimated mean kinematic vorticity numbers (W_m) within "A" thin sections by comparing our data to W_m contours plotted on a graph of Rs versus θ′ (Fig. 10D) (referred to here as the Rs-θ′ method; e.g., Tikoff and Fossen, 1995) (refer to discussion DR5 for evidence supporting assumptions for estimating W_m using this method). This method assumes that quartz clasts were homogeneously elongated in the direction of maximum finite stretching, which is supported by low SE values for Rs (typically ±0.1–0.2) and θ′ (typically ±3–6°) for each analysis. For estimation of W_m, idealized plane strain is assumed (e.g., Fossen and Tikoff, 1993; Johnson et al., 2009), and since most of the analyzed rocks experienced flattening strain, W_m values are here interpreted to represent maxima (e.g., Tikoff and Fossen, 1995). Given the relatively low strain magnitudes of our samples (total Rs range of 1.1–2.9), the overestimation of W_m likely does not exceed ~0.05 (Tikoff and Fossen, 1995). The range of W_m values reported for each sample was estimated from the ±1 SE θ′ error range (Fig. 10D; Table 4). Most samples (n = 21) yielded W_m values between 0.00 and 0.45 (70%–100% pure shear), with four outliers that yielded values as high as 0.65–0.85 (as little as 35%–55% pure shear).

The mean elongation direction of quartz porphyroclasts in "A" thin sections, as denoted by the sign of θ′, can also be used to determine shear-sense (e.g., Ramsay, 1967; Passchier and Trouw, 2006). Under our sign convention, negative θ′ values correspond to a top-to-NW shear-sense, and positive to top-to-SE (Fig. 10D). Most samples (n = 16) exhibit low (≤ ± 4°) θ′ values with error ranges that overlap with foliation, which we do not interpret as robust shear-sense indicators. However, the remaining nine samples exhibit θ′ values with error ranges that do not overlap with foliation. These include three Chekha Formation samples between +450 and +775 m (113, 89, 91) which define a top-to-NW shear sense, five Chekha Formation and TH samples between +1975 and +8775 m (97, 101, 46, 37, 36) that define a top-to-SE shear-sense, and a TH sample at +5700 m (45) that yielded a top-to-NW shear sense (Fig. 4).

Using methods outlined in Law (2010) and Xypolias et al. (2010), strain magnitude and W_m were integrated to calculate transport-parallel lengthening and flow plane-normal shortening (which is normal to the transport direction, and is from here on referred to as transport-normal shortening) for individual strain analyses (see Data Repository for additional information) (Table 4; Figs. 10E–10F). The data define an upward decrease in average lengthening and shortening for each strain domain. Domain 1 yielded an average lengthening value of 44 ± 5% (1 SE) and an average shortening value of 34 ± 2%. Domain 2 yielded average lengthening and shortening values of 20 ± 3% and 21 ± 2%, respectively. Domain 3 exhibits very low values, with 2 ± 1% lengthening and 3 ± 2% shortening. The average lengthening in the Y direction varies between 2% and 8% for all three strain domains.

DISCUSSION

Integration and Interpretation of Temperature and Structural Data Sets

The temperature, fabric, strain, and kinematic data sets allow generation of a structural model for the STDS in northwestern Bhutan. We interpret the base of the STDS zone, which we define as the section of rocks affected by deformation related to STDS shearing, at the onset of top-to-NW dominated shearing at −1825 m (Figs. 4 and 10G). This level coincides with the approximate base of prevalent (up to 30–40 vol%) granite sills. Quartz fabrics between −1550 and 0 m indicate approximately plane strain deformation, with well-developed CPO's that increase in cylindricity from 0.21 at −1550 m to 0.48–0.87 between −1325 and 0 m. Therefore, though no finite strain data are available from this interval,
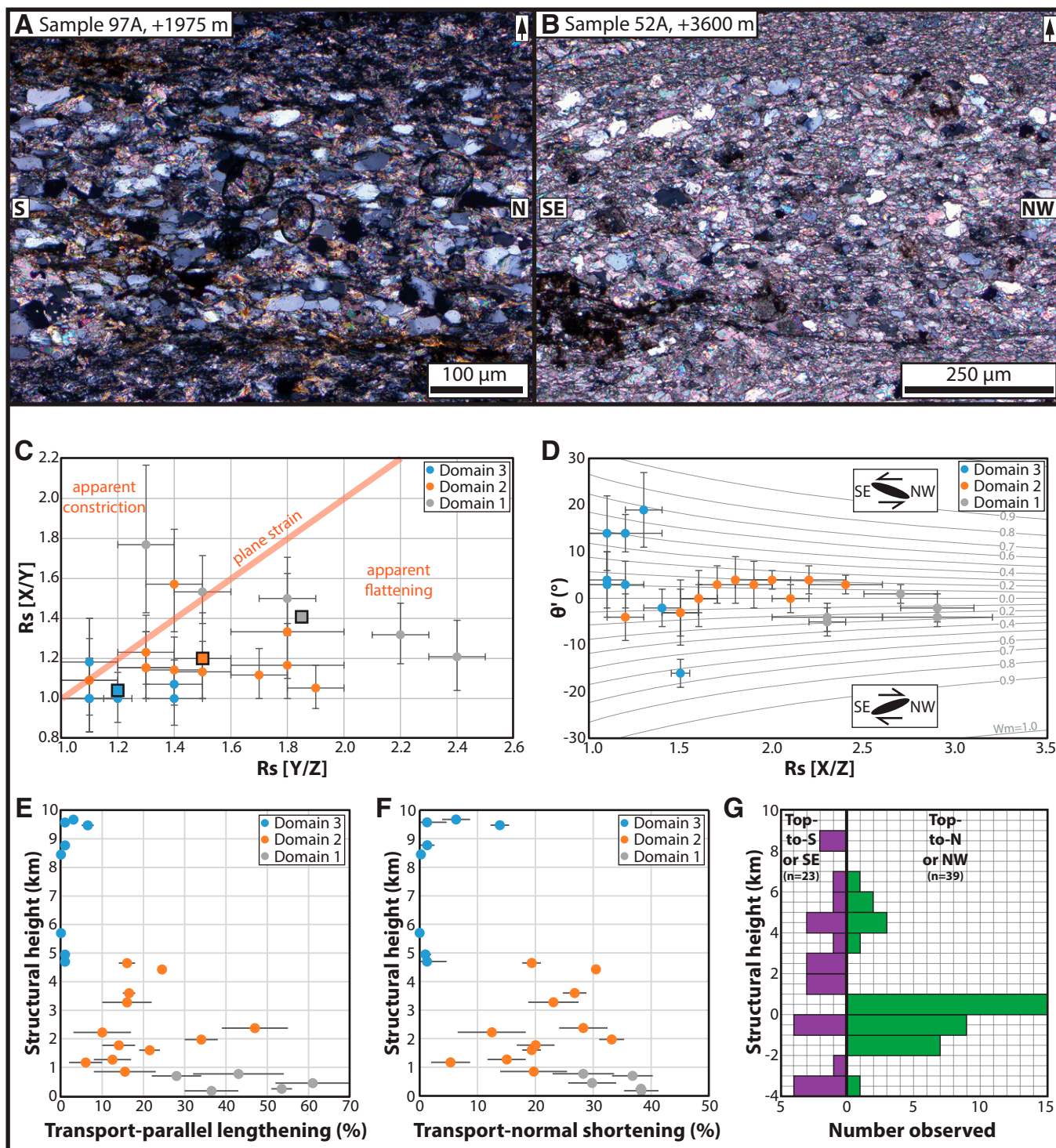
Figure 10. (A, B) Photomicrographs showing representative examples of non-recrystallized, elongated quartz porphyroclasts (i.e., relict, detrital grains) that were utilized for finite strain analyses (cross-polarized light; foliation oriented horizontal; arrow points structurally upward). Sample numbers are keyed to stops on Figs 2–4. (C) Flinn diagram (e.g., Flinn, 1962) showing 3-D strain fields for constant-volume deformation. Error bars are 1 standard error (SE). Boxes show average ellipsoid values for each strain domain. (D) Plot of tectonic elongation in "A" thin sections ($Rs_{[X/Z]}$) versus θ', with contours of mean kinematic vorticity for plane strain deformation (W_m) plotted (e.g., Tikoff and Fossen, 1995). Error bars are 1 SE. (E, F) Graphs of transport-parallel lengthening and transport-normal shortening versus structural height above the base of the Chekha Formation. (G) Frequency histogram of shear-sense indicators observed versus structural height relative to the base of the Chekha Formation.

TABLE 4. SUMMARY OF FINITE STRAIN DATA, KINEMATIC VORTICITY VALUES, SHEAR-SENSE, AND LENGTHENING AND SHORTENING MAGNITUDES FROM DODENA-LINGSHI TRANSECT SAMPLES

Sample	Map unit	Lithology	Structural height relative to base of Chekha Formation (m)	Foliation (d, dd)	Lineation (tr, pl)	Crenulation cleavage axis (tr, pl)	Orientation relative to lineation or crenulation	Thin section orientation (d, dd)	Rs (±1 SE)	φ (equal to θ') (±1 SE)	Strain domain	Shear-sense from Rs vs. θ' graph	Wm range from Rs vs. θ' method[1]	% Pure shear from Rs vs. θ' method[2]	Transport-parallel lengthening range (%)[3]	Transport-normal shortening range (%)[3]
33A	Cretaceous	Slate	9675	11, 225	–	12, 020	Normal to crenulation	84, 222	1.2 ± 0.1	3 ± 5	3	–	0.00–0.30	80–100%	2–4	4–9
33B							Parallel to crenulation	85, 112	1.2 ± 0.05	18 ± 6						
34A	Cretaceous	Graphitic slate	9575	38, 355	21, 300	–	Parallel to lineation	57, 220	1.1 ± 0.1	4 ± 6	3	–	0.00–0.35	75–100%	0–2	0–5
34B							Normal to lineation	67, 121	1.1 ± 0.1	10 ± 6						
35A	Cretaceous	Graphitic slate	9475	7, 324	13, 338	–	Parallel to lineation	89, 248	1.4 ± 0.1	−2 ± 4	3	–	0.00–0.25	80–100%	5–8	12–15
35B							Normal to lineation	87, 160	1.4 ± 0.1	−8 ± 4						
36A	Triassic–Jurassic	Graphitic slate	8775	19, 155	9, 201	–	Parallel to lineation	74, 298	1.1 ± 0.1	14 ± 8	3	top-to-SW	0.20–0.70	50–85%	0–2	0–3
36B							Normal to lineation	77, 021	1.1 ± 0.1	11 ± 9						
37A	Triassic–Jurassic	Graphitic slate	8450	75, 352	64, 298	–	Parallel to lineation	69, 259	1.3 ± 0.1	19 ± 8	3	top-to-SE	0.45–0.85	35–70%	0	0
37B							Normal to lineation	27, 127	1.1 ± 0.1	10 ± 6						
45A	Paleozoic	Quartzite	5700	16, 322	16, 316	–	Parallel to lineation	87, 227	1.5 ± 0.05	−16 ± 3	3	top-to-NW	0.55–0.75	45–60%	0	0
45B							Normal to lineation	74, 147	1.4 ± 0.1	17 ± 6						
46A	Chekha	Marble	4950	40, 350	40, 342	–	Parallel to lineation	86, 256	1.1 ± 0.1	−11 ± 8	3	top-to-SE	0.35–0.65	55–75%	0–2	0–2
46B							Normal to lineation	51, 164	1.2 ± 0.2	14 ± 4						
48A	Chekha	Marble	4700	25, 325	22, 293	–	Parallel to lineation	82, 209	1.1 ± 0.1	3 ± 7	3	–	0.00–0.35	75–100%	0–2	0–5
48B							Normal to lineation	69, 114	1.1 ± 0.1	17 ± 5						
49A	Chekha	Marble	4650	44, 356	16, 315	–	Parallel to lineation	61, 233	1.6 ± 0.1	0 ± 6	2	–	0.00–0.25	80–100%	14–18	18–21
49B							Normal to lineation	56, 136	1.4 ± 0.1	6 ± 4						
50A	Chekha	Phyllite	4425	5, 050	1, 334	5, 043	Parallel to lineation	86, 243	1.8 ± 0.2	−5 ± 4	2	–	0.00–0.15	90–100%	24–25	30–31
50B							Normal to lineation	90, 152	2.1 ± 0.1	0 ± 3						
52A	Chekha	Marble	3600	21, 355	14, 309	–	Parallel to lineation	73, 221	2.0 ± 0.1	4 ± 2	2	–	0.10–0.30	80–95%	15–18	25–29
52B							Normal to lineation	76, 130	1.9 ± 0.1	−6 ± 3						
53A	Chekha	Marble	3275	41, 334	41, 292	–	Parallel to lineation	66, 216	1.9 ± 0.1	3 ± 5	2	–	0.00–0.40	70–100%	10–22	19–27
53B							Normal to lineation	58, 111	1.7 ± 0.1	16 ± 4						
101A	Chekha	Calcareous phyllite	2375	20, 290	0, 020	19, 260	Parallel to lineation	71, 110	2.2 ± 0.2	4 ± 3	2	top-to-SW	0.05–0.40	70–95%	39–55	24–32
101B							Normal to lineation	88, 200	1.4 ± 0.1	−8 ± 4						
99A	Chekha	Marble	2225	9, 265	2, 335	–	Parallel to lineation	82, 064	1.5 ± 0.1	−3 ± 7	2	–	0.00–0.45	70–100%	3–17	7–18
99B							Normal to lineation	87, 157	1.3 ± 0.1	42 ± 6						
97A	Chekha	Phyllitic quartzite	1975	22, 235	17, 192	–	Parallel to lineation	76, 108	2.4 ± 0.2	3 ± 2	2	top-to-SW	0.05–0.30	80–95%	30–38	31–35
97B							Normal to lineation	74, 011	1.8 ± 0.2	−1 ± 4						
95A	Chekha	Marble	1775	12, 230	–	12, 246	Normal to crenulation	88, 065	1.7 ± 0.1	3 ± 4	2	–	0.00–0.35	75–100%	10–18	17–23
95B							Parallel to crenulation	87, 335	1.5 ± 0.1	−6 ± 4						
93A	Chekha	Marble	1600	26, 275	26, 281	–	Parallel to lineation	89, 010	1.6 ± 0.1	0 ± 3	2	–	0.00–0.25	85–100%	19–24	18–21
93B							Normal to lineation	64, 103	1.3 ± 0.1	−8 ± 6						
105A	Chekha	Marble	1275	25, 240	17, 007	–	Parallel to lineation	71, 103	1.5 ± 0.1	−3 ± 5	2	–	0.00–0.35	75–100%	8–17	12–18
105B							Normal to lineation	76, 006	1.3 ± 0.1	0 ± 5						
108A	Chekha	Marble	1175	16, 165	–	2, 084	Normal to crenulation	85, 265	1.2 ± 0.1	−4 ± 5	2	–	0.00–0.35	75–100%	2–10	2–9
108B							Parallel to crenulation	75, 354	1.1 ± 0.1	−3 ± 4						
110A	Chekha	Marble	850	10, 310	7, 281	–	Parallel to lineation	85, 194	1.8 ± 0.2	4 ± 5	2	–	0.00–0.45	70–100%	8–23	14–25
110B							Normal to lineation	82, 101	1.5 ± 0.1	0 ± 6						
91A	Chekha	Schist	775	10, 220	5, 155	6, 277	Parallel to lineation	81, 065	2.3 ± 0.1	−5 ± 3	1	top-to-NW	0.10–0.45	70–95%	3–-54	23–34
91B							Normal to lineation	87, 345	1.5 ± 0.1	9 ± 5						
89A	Chekha	Calcareous quartzite	700	14, 250	10, 172	–	Parallel to lineation	76, 084	2.9 ± 0.3	−4 ± 2	1	top-to-N	0.15–0.40	70–90%	22–34	33–40
89B							Normal to lineation	87, 351	2.4 ± 0.1	−2 ± 3						
113A	Chekha	Calc-silicate gneiss	450	16, 215	8, 153	–	Parallel to lineation	76, 064	2.3 ± 0.3	−4 ± 3	1	top-to-NW	0.05–0.40	70–95%	52–70	26–34
113B							Normal to lineation	83, 333	1.3 ± 0.1	6 ± 8						
84A	Chekha	Schist	250	11, 215	10, 184	–	Parallel to lineation	84, 095	2.7 ± 0.2	1 ± 2	1	–	0.00–0.20	85–100%	51–56	37–39
84B							Normal to lineation	81, 005	1.8 ± 0.1	3 ± 4						
83A	Chekha	Calc-silicate gneiss	175	17, 340	17, 345	–	Parallel to lineation	89, 255	2.9 ± 0.2	−2 ± 3	1	–	0.00–0.35	75–100%	30–43	35–41
83B							Normal to lineation	73, 168	2.2 ± 0.1	0 ± 3						

Note: SE—standard error; d, dd—dip, dip direction notation; tr, pl—trend, plunge notation. Rs—tectonic elongation (long axis to short axis ratio); φ—angle between long axis and foliation (equal to θ' of Ramsay and Huber, 1983); (sign convention for φ: clockwise from foliation is positive, counterclockwise from foliation is negative); Wm—mean kinematic vorticity number. GPS locations of all samples are shown on Table DR1 (text footnote 1).
[1]Estimated Wm values are rounded to nearest 0.05.
[3]Calculated using the equations from Figure 10 of Law (2010); see Data Repository for additional information on methodology.

the gradient in fabric intensity observed between quartz-rich samples of similar lithology implies an upward-increasing strain gradient (Fig. 11B) (e.g., Larson et al., 2017). Most W_m values in this interval range from 0.74 to 0.88, indicating a dominance (55%–70%) of simple shear. Published pressure data from GH samples at −1000 m (9.0 ± 0.8 kbar), −550 m (6.9 ± 1.5 kbar), and −50 m (6.2 ± 1.7 kbar) (Kellett et al., 2010) define a best-fit, upright field gradient of 2.92 ± 0.94 kbar/km (R^2 = 0.91). This is ~7–14 times steeper than a typical lithostatic gradient for mid-crustal rocks of 0.27 kbar/km, and corresponds to 86%–93% apparent vertical shortening (Fig. 11B). This shortening range is similar to other estimates across the STDS in the Everest region (90%–94%; Law et al., 2011) and in northwestern India (96%; Herren, 1987). The pressure data indicate that at least ~6–13 km of apparent structural thinning was accommodated within the basal 1.8 km of the STDS zone. When integrated with W_m data, this thinning appears to have been accomplished dominantly by simple shear (55%–70%) with a less significant component of shortening normal to the shear zone boundaries. To accomplish this, the shear zone must have dipped northward while it was active (e.g., Law et al., 2011). Using a simple geometric model that attributes 55%–70% of the structural thinning to simple shear, offset ranges of 30–38 km and 59–76 km can account for the pressure difference between GH samples at −1000 and −50 m for a shear zone active at a dip angle of 10° and 5°, respectively. This corresponds to a range of shear strain values between 5.7 and 11.4. These offset ranges should be considered minima, as they were calculated to account for the pressure difference between samples that do not encompass the complete thickness of the basal part of the STDS zone.

Between −1100 and +700 m, many samples exhibit evidence for quartz recrystallization at temperatures up to ~100 to ~250 °C lower than peak temperatures (Fig. 4), as constrained by quartz fabric opening angles and semiquantitative bracketing using quartz recrystallization microstructures. Because of the difference between peak and deformation temperatures, we interpret these fabrics to have been generated along the exhumation path (e.g., Law, 2014), and therefore likely represent recrystallization during the later stages of shearing on the STDS. This interpretation is further supported by the dominance of top-to-NW shear-sense indicators and

quartz fabrics within this interval, which also argue for recrystallization along the exhumation path (e.g., Law et al., 2011).

The peak metamorphic temperature data define two intervals with telescoped isotherms, one between −50 and +1275 m, and the other between +1975 and +3050 m (Fig. 4). We interpret the upward increase from ~450 to ~620 °C between +1275 and +1975 m to be the result of structural repetition of part of the Chekha Formation by an intraformational thrust fault or thrust-sense shear zone that post-dates STDS movement. Several lines of evidence support this interpretation, including: (1) the Chekha Formation is anomalously thick along this transect compared to other areas of the Lingshi exposure or farther east in Bhutan, where it typically ranges between ~1000 and 2000 m thick (Gansser, 1983; Kellett et al., 2009, 2010; Long et al., 2011a, 2011c; Kellett and Grujic, 2012); (2) Kellett and Grujic (2012) inferred a S-vergent thrust fault in their cross section through the Linghsi exposure (their fig. 3B), which projects to an approximate structural height of +1650 m and therefore lies within the location range proposed here; (3) Gansser (1983) also speculated that thrust faults had thickened the Chekha Formation marble along this transect; and (4) south-vergent thrusting that is interpreted to post-date shearing on the STDS has been documented across northern Bhutan (Grujic et al., 2002, 2011; Kellett et al., 2009; Warren et al., 2011). Therefore, we suggest that the observed thermal pattern is most likely the result of thrust repetition of telescoped isotherms produced during earlier shearing on the STDS. By restoring sample 97 to the level of sample 89, which both have similar peak temperatures of ~625 °C, structural repetition of ~1300 m of the Chekha Formation is estimated.

We interpret the boundary between strain domains 2 and 3 at ~4.7 km above the base of the Chekha Formation, which represents an upward transition to very low strain magnitudes (Rs ~1.25), as the approximate top of the STDS zone (Fig. 11B). This defines a present-day thickness of 6.5 km for the STDS zone, which restores to an original thickness of ~5.2 km after accounting for post-STDS thrust repetition. The cumulative temperature decrease across the STDS zone is ~300–400 °C (from ~625–725 to ~325 °C). This is similar to temperature patterns documented across the STDS in the Everest region, where Cottle et al. (2011) measured an upward decrease from ~650 to ~340 °C across an ~1-km-thick STDS
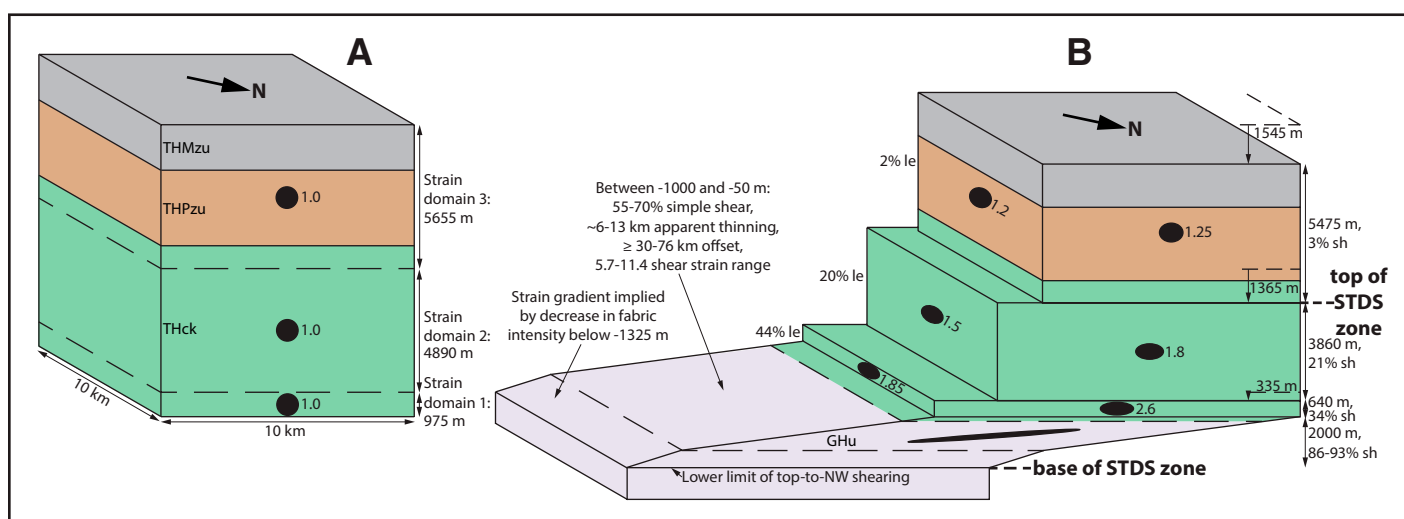

Figure 11. (A, B) Diagrams illustrating the change in dimensions (le—transport-parallel lengthening; sh—transport-normal shortening) of a 10 km x 10 km area of the Chekha Formation (THck) and Paleozoic (THPzu) and Mesozoic Tethyan Himalayan rocks (THMzu) before (A) and after (B) the measured finite strain (assuming homogeneous strain magnitudes across- and along-strike). Diagram B also shows a schematic representation of high-magnitude, simple shear-dominated offset within Greater Himalayan rocks (GHu) in the lower part of the South Tibetan detachment system (STDS) zone.

zone, and Law et al. (2011) measured an upward decrease from ~680 to ~460 °C across an ~0.5-km-thick STDS zone.

The finite strain data from TH rocks define a downward-increasing gradient in transport-parallel lengthening, which indicates that a component of top-to-NW displacement is broadly distributed through the upper part of the STDS zone (Fig. 11A, 11B). This is compatible with shear-sense observations, which indicate top-to-NW shearing as high as +3–7 km (Fig. 10G). Between the base of strain domain 3 (+4.7 km) and the top of domain 1 (+0.8 km), a 42% difference in lengthening is observed. A minimum NW-SE map length of ~50 km of the Chekha Formation is preserved in northwestern Bhutan (Fig. 1C). Using this length, and assuming that strain magnitudes were similar across-strike, this corresponds to a minimum of ~21 km of differential lengthening distributed through the upper part of the STDS zone. Therefore, the upper part of the STDS acted as a stretching fault (e.g., Means, 1989; Grujic et al., 2002), and pure shear-dominated lengthening contributed at least a few 10s of km to its overall offset magnitude.

The finite strain and vorticity data from TH rocks, when combined with the fabric, vorticity, and pressure data from GH rocks, can be used to divide the STDS zone into two distinct levels: (1) a lower level (−1825 to +175 m) dominated by simple shear, which accommodated significant apparent thinning (>6–13 km); and (2) an upper level (+175 to +4675 m) characterized by distributed, pure shear-dominated lengthening and shortening, which both progressively decrease upward (lengthening from 44% to 2%, and shortening from 34% to 3%) (Fig. 11B). Offset magnitude varies significantly between the two levels, with ~20 km of distributed top-to-NW displacement accommodated in the upper level, and at least ~30–75 km accommodated by simple shear in the lower level. These estimates are compatible with finite strain data in central Bhutan, which allow for up to ~85 km of distributed N-vergent shearing that may have been fed northward into the STDS (Long et al., 2017). Studies in other areas of the Himalaya have estimated offset magnitudes of a similar order. In the Everest region, barometric gradients (Searle et al., 2002, 2003), telescoped isotherms (Law et al., 2011), and peak temperatures above and below the shear zone (Cottle et al., 2007, 2011) have yielded STDS offset ranges of ~90–216 km, ~25–170 km, and ~15–67 km, respectively. In northwestern India, offset on the Zanskar shear zone, a western equivalent of the STDS, has been estimated between ~25 and ~120 km (Herren, 1987; Dèzes et al., 1999; Walker et al., 1999).

One interesting observation is that telescoped isotherms are located entirely within the gently shortened upper level of the STDS zone, and not within the highly thinned lower level, and thus appear to be spatially decoupled from strain magnitude. We suggest that isotherms were progressively elevated and compressed as a result of long-lived, distributed intrusion of granite sills during STDS shearing, which record crystallization spanning from ca. 24 to ca. 16 Ma (Kellett et al., 2009). A similar interpretation of significant heat contribution from granite sill injection during shearing has also been proposed for the STDS in the Everest region (Waters et al., 2018).

Evolution of the STDS in Northwestern Bhutan

The interpretations outlined above, when combined with timing constraints for metamorphism, granite intrusion, and shearing on the STDS from Kellett et al. (2009, 2010), define the following order of events (Fig. 12).

(1) 26–22 Ma: pre-STDS shearing (Fig. 12A): GH rocks that will eventually occupy the footwall and lower level of the STDS zone were buried to ~9 kbar (~35 km), and attained peak temperatures of ~650–725 °C (Kellett et al., 2010; this study). Much of the burial of GH rocks can likely

be attributed to construction of a south-vergent Paleogene thrust belt in overlying TH rocks, as documented in several places in southern Tibet (e.g., Ratschbacher et al., 1994; Wiesmayr and Grasemann, 2002; Murphy and Yin, 2003; Aikman et al., 2008). Prograde growth of monazite in GH rocks in northwestern Bhutan took place between ca. 26 and ca. 21 Ma, and peak metamorphism and partial melting are interpreted at ca. 22–23 Ma (Kellett et al., 2010). This brackets the earliest possible timing of shearing on the STDS. The Chekha Formation, which will eventually occupy the upper level of the STDS zone, attained peak temperatures of ~300–350 °C, as indicated from the non-elevated "background" temperatures near the top of the section.

(2) 22–16 Ma: initial STDS shearing (Fig. 12B): Initial shearing was accompanied by retrograde growth of monazite in GH rocks from ca. 19 to ca. 15 Ma (Kellett et al., 2010), and intrusion and solid-state deformation of granite sills throughout the STDS zone, which crystallized between ca. 24 and ca. 16 Ma (Kellett et al., 2009). GH rocks in the lower level of the STDS zone accommodated high-magnitude, simple shear-dominated offset, which resulted in significant apparent thinning. Early, high-temperature quartz recrystallization microstructures (CBE, GBM) were generated while GH rocks were still >550 °C. In the upper level of the STDS zone, distributed top-to-NW offset was accommodated by an upward-decreasing gradient in pure shear-dominated lengthening. Protracted, spatially dense intrusion of granite sills (and also larger granite bodies, such as observed ~20 km to the west of the studied transect; Fig. 1C) between ca. 24 and ca. 16 Ma enhanced temperatures throughout the STDS zone during shearing, eventually resulting in elevation and compression of isotherms into a relatively thin interval that lies entirely within the Chekha Formation.

(3) 16–>11 Ma: late-stage STDS shearing (Fig. 12C): Far along the exhumation path, quartz microstructures indicating SGR recrystallization were generated within the lower level of the STDS zone, while GH rocks were between ~450 and 550 °C. A granite sill in the Chekha Formation cooled through ~425 °C by ca. 11 Ma (Kellett et al., 2009), potentially bracketing the timing of development of SGR microstructures.

(4) 15–11 Ma: post-STDS thrusting (Fig. 12D): Motion on a top-to-S thrust fault that post-dated STDS shearing repeated a portion of the Chekha Formation section that contains the telescoped field gradient. The interpreted timing range is based on out-of-sequence thrusting documented across northern Bhutan (the Kakhtang and Laya thrusts), which is bracketed between ca. 15 and ca. 11 Ma (Grujic et al., 2002, 2011; Kellett et al., 2009; Warren et al., 2011).

Implications for Definition of the STDS Zone and Other Shear Zones

One interesting finding of our study is that the interval of telescoped isotherms lies entirely above the level of the STDS zone that experienced the highest offset magnitude and greatest apparent thinning (Figs. 11B, 12B, and 12C). This emphasizes the importance of defining shear zone boundaries on the basis of structural and/or kinematic criteria, and not exclusively on the spatial limits of metamorphic field gradients. This is in agreement with several studies that argue that defining the limits of a zone of high strain is the best way to delineate shear zone boundaries (e.g., Ramsay and Graham, 1970; Ramsay, 1980; White et al., 1980; Ramsay and Huber, 1983; Means, 1995; Searle et al., 2008).

As the STDS represents a top-to-N structure within an overall top-to-S orogen, it is tempting to use the limits of top-to-N shear-sense indicators to define its boundaries. However, we observed top-to-N indicators over a >10 km structural thickness (Fig. 10G), and top-to-N and top-to-S indicators are interspersed through an ~11-km-thick section of GH and TH
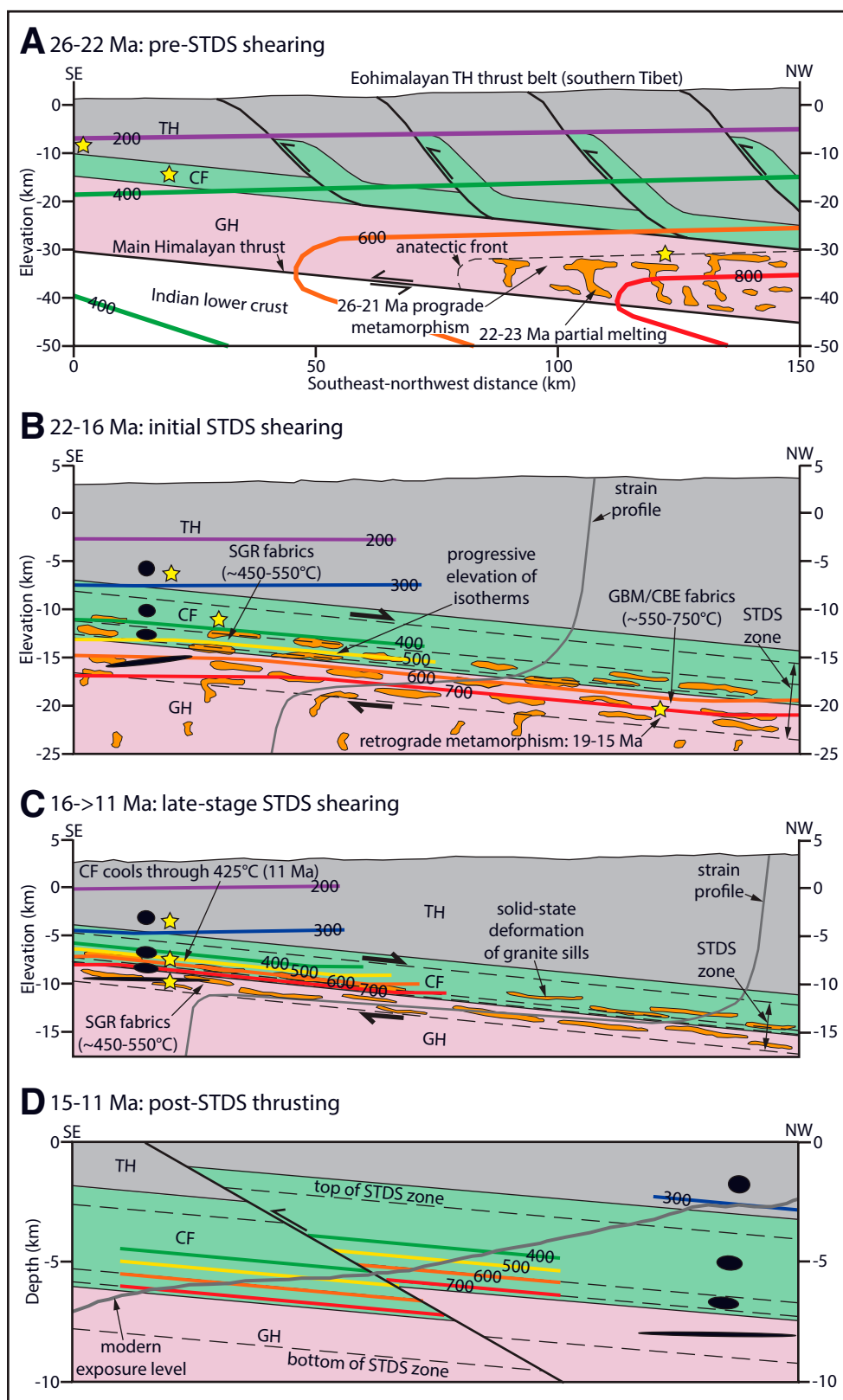
Figure 12. Schematic diagrams of the evolution of the South Tibetan detachment system (STDS) in northwestern Bhutan. TH—Tethyan Himalayan rocks; CF—Chekha Formation; GH—Greater Himalayan rocks. Yellow stars indicate rocks that will eventually be juxtaposed by motion on the STDS. (A) 26–22 Ma: Subduction of GH protoliths to mid-crustal levels is attributed to burial below an Eohimalayan (Paleogene) thrust belt constructed in TH rocks in southern Tibet (e.g., Ratschbacher et al., 1994; Wiesmayr and Grasemann, 2002; Murphy and Yin, 2003; Aikman et al., 2008). Schematic steady-state isotherms are shown (after Henry et al., 1997). (B) 22–16 Ma: High-magnitude simple shear was accommodated in the lower level of the STDS zone, and pure shear-dominated lengthening was distributed through the upper level. Shearing was accompanied by protracted intrusion of granite sills, which progressively elevated isotherms into the upper level of the STDS zone (schematic isotherms represent the peak temperature conditions recorded at any given structural level, which locally may have been attained prior to this increment). SGR, GBM, and CBE represent subgrain rotation, grain boundary migration, and chessboard extinction quartz microstructures, respectively. (C) 16–>11 Ma: Late-stage SGR recrystallization microstructures were generated within the lower level of the STDS zone, and the CF cooled through ~425 °C by ca. 11 Ma (isotherms represent peak temperatures, as in diagram B). (D) 15–11 Ma: Motion on a top-to-S, post-STDS, intraformational thrust fault repeated of a portion of the telescoped thermal field gradient in the CF (isotherms represent peak temperatures, as in diagrams B and C). The geometry shown for the thrust fault is schematic; many geometries are possible.

rocks in central Bhutan (Long et al., 2011b, 2017). Though we do map the base of the STDS zone at the onset of dominant top-to-N shearing, this is corroborated by an upward increase in fabric intensity that we interpret to represent a gradient in strain magnitude (e.g., Larson et al., 2017). We define the top of the STDS zone using a gradient in thin section-scale finite strain magnitude. Therefore, this case study demonstrates the utility of using a combination of quantitative fabric and finite strain analyses to delineate shear zone boundaries in situations where structural criteria indicative of strain gradients may not be easily identifiable in the field.

CONCLUSIONS

1. We divide the STDS in NW Bhutan into an ~2-km-thick lower level that accommodated ~6–13 km of apparent structural thinning (86%–93% shortening) through high-magnitude (≥30–76 km), simple shear-dominant (W_m = 0.74–0.88), top-to-NW displacement, and an ~3-km-thick upper level that accommodated ≥21 km of top-to-NW displacement via an upward decrease (from 44% to 2%) in pure shear-dominant (W_m = 0.00–0.45), transport-parallel lengthening.

2. Peak temperatures within and beneath the lower level of the STDS zone are ~650–750 °C. Two intervals of telescoped upright isotherms are observed in the upper level of the STDS zone, and define ~160–260 °C/km field gradients. The lower interval is 1.3 km thick, and exhibits an upward decrease from ~700 to ~450 °C. Above this, temperatures increase abruptly from ~450 to ~620 °C, which is interpreted as the result of post-STDS thrust repletion. Moving structurally upward, temperatures decrease from ~620 to ~320 °C over a 1.1-km-thick interval, and temperatures decrease gradually from ~320 to ~250 °C through a 7-km-thick section of overlying TH rocks.

3. Telescoped isotherms are located above the highly thinned lower level of the STDS zone, and therefore are spatially decoupled from strain magnitude. We interpret this to be a consequence of isotherm elevation during distributed granite intrusion that spanned the duration of STDS shearing. This work highlights the importance of defining shear zone boundaries on the basis of structural criteria, and not relying exclusively on the spatial limits of metamorphic field gradients. In addition, this study demonstrates the utility of using fabric and finite strain analyses to delineate shear zone boundaries when field criteria may not be available.

REFERENCES CITED

Aikman, A.B., Harrison, T.M., and Ding, L., 2008, Evidence for early (>44 Ma) Himalayan crustal thickening, Tethyan Himalaya, southeastern Tibet: Earth and Planetary Science Letters, v. 274, p. 14–23, https://doi.org/10.1016/j.epsl.2008.06.038.

Allmendinger, R.W., Cardozo, N., and Fisher, D., 2011, Structural geology algorithms: Vectors and tensors in structural geology: New York, USA, Cambridge University Press, 304 p., https://doi.org/10.1017/CBO9780511920202.

Antolín, B., Schill, E., Grujic, D., Baule, S., Quidelleur, X., Appel, E., and Waldhör, M., 2012, E-W extension and block rotation of the southeastern Tibet: Unravelling late deformation stages in the eastern Himalayas (NW Bhutan) by means of pyrrhotite remanences: Journal of Structural Geology, v. 42, p. 19–33, https://doi.org/10.1016/j.jsg.2012.07.003.

Armijo, R., Tapponnier, P., Mercier, J., and Tong-Lin, H., 1986, Quaternary extension in southern Tibet: Field observations and tectonic implications: Journal of Geophysical Research. Solid Earth, v. 91, p. 13803–13872, https://doi.org/10.1029/JB091iB14p13803.

Bailey, J.E., and Hirsch, P.B., 1962, The recrystallization process in some polycrystalline metals: Proclamations of the Royal Society of London, serial A267, p. 11–30.

Barth, N., Hacker, B., Seward, G., Walsh, E., Young, D., and Johnston, S., 2010, Strain within the ultrahigh-pressure Western Gneiss region of Norway recorded by quartz CPOs, in Law, R.D., Butler, R.W.H., Holdsworth, R., Krabbendam, M., and Strachan R.A., eds.,

Continental Tectonics and Mountain Building: The Legacy of Peach and Horne: Geological Society of London Special Publication, v. 335, p. 663–685, https://doi.org/10.1144/SP335.27.

Beaumont, C., Jamieson, R.A., Nguyen, M.H., and Lee, B., 2001, Himalayan tectonics explained by extrusion of a low-viscosity crustal channel coupled to focused surface denudation: Nature, v. 414, p. 738–742, https://doi.org/10.1038/414738a.

Beaumont, C., Jamieson, R.A., Nguyen, M.H., and Medvedev, S., 2004, Crustal channel flows: 1. Numerical models with applications to the tectonics of the Himalayan-Tibetan orogen: Journal of Geophysical Research. Solid Earth, v. 109, no. B6, https://doi.org/10.1029/2003JB002809.

Behrmann, H.H., and Platt, J.P., 1982, Sense of nappe emplacement from quartz c-axis fabrics: An example from the Betic Cordilleras (Spain): Earth and Planetary Science Letters, v. 59, p. 208–215, https://doi.org/10.1016/0012-821X(82)90126-1.

Beyssac, O., Goffe, B., Chopin, C., and Rouzaud, J., 2002, Raman spectra of carbonaceous material in metasediments: A new geothermometer: Journal of Metamorphic Geology, v. 20, p. 859–871, https://doi.org/10.1046/j.1525-1314.2002.00408.x.

Beyssac, O., Goffe, B., Petitet, J.P., Froigneux, E., Moreau, M., and Rouzaud, J.N., 2003, On the characterization of disordered and heterogeneous carbonaceous materials by Raman spectroscopy: Spectrochimica Acta Part A, v. 59, p. 2267–2276, https://doi.org/10.1016/S1386-1425(03)00070-2.

Bhargava, O.N., 1995, The Bhutan Himalaya: A Geological Account: Geological Survey of India, Special Publication Series, v. 39, 245 p.

Bouchez, J.L., Lister, G.S., and Nicolas, A., 1983, Fabric asymmetry and shear sense in movement zones: Geologische Rundschau, v. 72, p. 401–419, https://doi.org/10.1007/BF01822075.

Brookfield, M.E., 1993, The Himalayan passive margin from Precambrian to Cretaceous times: Sedimentary Geology, v. 84, p. 1–35, https://doi.org/10.1016/0037-0738(93)90042-4.

Burchfiel, B.C., and Royden, L.H., 1985, North-south extension within the convergent Himalayan region: Geology, v. 13, p. 679–682, https://doi.org/10.1130/0091-7613(1985)13<679:NEWTCH>2.0.CO;2.

Burchfiel, B.C., Chen, Z.L., Hodges, K.V., Liu, Y.P., Royden, L.H., Deng, C.R., and Xu, J.N., 1992, The South Tibetan detachment system, Himalayan Orogen: Extension contemporaneous with and parallel to shortening in a collisional mountain belt: Geological Society of America Special Paper 269, 41 p.

Burg, J.P., 1983, Tectogenese compare de deux segments de chaine de collision: Le sud du Tibet (suture du Tsangpo), la chaine hercynienne en Europe (suture du Massif Central) [thesis]: Montpellier, France, University of Montpellier, 450 p.

Burg, J.P., and Chen, G.M., 1984, Tectonics and structural zonation of southern Tibet, China: Nature, v. 311, p. 219–223, https://doi.org/10.1038/311219a0.

Cooper, F.J., Hodges, K.V., and Adams, B.A., 2013, Metamorphic constraints on the character and displacement of the South Tibetan fault system, central Bhutanese Himalaya: Lithosphere, v. 5, p. 67–81, https://doi.org/10.1130/L221.1.

Cooper, F.J., Hodges, K.V., Parrish, R.R., Roberts, N.M.W., and Horstwood, M.S.A., 2015, Synchronous N-S and E-W extension at the Tibet-to-Himalaya transition in NW Bhutan: Tectonics, v. 34, p. 1375–1395, https://doi.org/10.1002/2014TC003712.

Corrie, S.L., and Kohn, M.J., 2011, Metamorphic history of the central Himalaya, Annapurna region, Nepal, and implications for tectonic models: Geological Society of America Bulletin, v. 123, p. 1863–1879, https://doi.org/10.1130/B30376.1.

Cottle, J.M., Jessup, M.J., Newell, D.J., Searle, M.P., Law, R.D., and Horstwood, M.S., 2007, Structural insights into the early stages of exhumation along an orogen-scale detachment: The South Tibetan Detachment System, Dzakaa Chu section, Eastern Himalaya: Journal of Structural Geology, v. 29, p. 1781–1797, https://doi.org/10.1016/j.jsg.2007.08.007.

Cottle, J.M., Waters, D.J., Riley, D., Beyssac, O., and Jessup, M.J., 2011, Metamorphic history of the south Tibetan detachment system, Mt. Everest region, revealed by RSCM thermometry and phase equilibria modeling: Journal of Metamorphic Geology, v. 29, p. 561–582, https://doi.org/10.1111/j.1525-1314.2011.00930.x.

Cottle, J.M., Larson, K.P., and Kellett, D.A., 2015, How does the mid-crust accommodate deformation in large, hot collisional orogens? A review of recent research in the Himalayan orogen: Journal of Structural Geology, v. 78, p. 119–133, https://doi.org/10.1016/j.jsg.2015.06.008.

DeCelles, P.G., Gehrels, G.E., Quade, J., Kapp, P.A., Ojha, T.P., and Upreti, B.N., 1998, Neogene foreland basin deposits, erosional unroofing, and the kinematic history of the Himalayan fold-thrust belt, western Nepal: Geological Society of America Bulletin, v. 110, p. 2–21, https://doi.org/10.1130/0016-7606(1998)110<0002:NFBDEU>2.3.CO;2.

Dèzes, P.J., Vannay, J.-C., Steck, A., Bussy, F., and Cosca, M., 1999, Synorogenic extension, quantitative constraints on the age and displacement of the Zanskar Shear Zone (northwest Himalaya): Geological Society of America Bulletin, v. 111, p. 364–374, https://doi.org/10.1130/0016-7606(1999)111<0364:SEQCOT>2.3.CO;2.

Drury, M.R., Humphreys, F.J., and White, S.H., 1985, Large strain deformation studies using polycrystalline magnesium as rock analogue, Part II: Dynamic recrystallization mechanisms at high temperatures: Physics of the Earth and Planetary Interiors, v. 40, p. 208–222, https://doi.org/10.1016/0031-9201(85)90131-1.

Dunnet, D., 1969, A technique for finite strain analysis using elliptical particles: Tectonophysics, v. 7, p. 117–136, https://doi.org/10.1016/0040-1951(69)90002-X.

Edwards, M.A., Kidd, W.S.F., Li, J., Yue, Y., and Clark, M., 1996, Multi-stage development of the southern Tibet detachment system near Khula Kangri: New data from Gonto La: Tectonophysics, v. 260, p. 1–19, https://doi.org/10.1016/0040-1951(96)00073-X.

Edwards, M.A., Pecher, A., Kidd, W.S.F., Burchfiel, B.C., and Royden, L.H., 1999, Southern Tibet detachment system at Khula Kangri, eastern Himalaya: A large-area, shallow detachment stretching into Bhutan?: The Journal of Geology, v. 107, p. 623–631, https://doi.org/10.1086/314366.

England, P., and Molnar, P., 1993, Cause and effect among thrust and normal faulting, anatectic melting and exhumation in the Himalaya, in Treloar, P.J., and Searle, M.P., eds., Himalayan Tectonics: Geological Society of London Special Publication 74, p. 401–411, https://doi.org/10.1144/GSL.SP.1993.074.01.27.

Faleiros, F.M., Moraes, R., Pavan, M., and Campanha, G.A.C., 2016, A new empirical calibration of the quartz c-axis fabric opening-angle deformation thermometer: Tectonophysics, v. 671, p. 173–182, https://doi.org/10.1016/j.tecto.2016.01.014.

Flinn, D., 1962, On folding during three-dimensional progressive deformation: Quarterly Journal of the Geological Society of London, v. 118, p. 385–428, https://doi.org/10.1144/gsjgs.118.1.0385.

Fossen, H., and Tikoff, B., 1993, The deformation matrix for simultaneous simple shearing, pure shearing and volume change, and its application to transpression-transtension tectonics: Journal of Structural Geology, v. 15, p. 413–422, https://doi.org/10.1016/0191-8141(93)90137-Y.

Ganesan, T.M., and Bose, M.N., 1982, Plant remains of Mesozoic age from Lingshi Basin, Bhutan: Geophytology, v. 12, p. 279–286.

Gansser, A., 1964, Geology of the Himalayas: New York, USA, Wiley-Interscience, 289 p.

Gansser, A., 1983, Geology of the Bhutan Himalaya: Basel, Switzerland, Birkäuser, 181 p.

Garzanti, E., 1999, Stratigraphy and sedimentary history of the Nepal Tethys Himalaya passive margin: Journal of Asian Earth Sciences, v. 17, p. 805–827, https://doi.org/10.1016/S1367-9120(99)00017-6.

Godin, L., Parrish, R.R., Brown, R.L., and Hodges, K.V., 2001, Crustal thickening leading to exhumation of the Himalayan metamorphic core of central Nepal: Insight from U-Pb geochronology and $^{40}Ar/^{39}Ar$ thermochronology: Tectonics, v. 20, p. 729–747, https://doi.org/10.1029/2000TC001204.

Godin, L., Grujic, D., Law, R.D., and Searle, M.P., 2006, Channel flow, ductile extrusion and exhumation in continental collision zones: An introduction, in Law, R., Searle, M.P., and Godin, L., eds., Channel Flow, Ductile Extrusion and Exhumation in Continental Collision Zones: Geological Society of London Special Publication 268, p. 1–23, https://doi.org/10.1144/GSL.SP.2006.268.01.01.

Grujic, D., Casey, M., Davidson, C., Hollister, L.S., Kundig, R., Pavlis, T., and Schmid, S., 1996, Ductile extrusion of the Higher Himalayan Crystallines in Bhutan: Evidence from quartz microfabrics: Tectonophysics, v. 260, p. 21–43, https://doi.org/10.1016/0040-1951(96)00074-1.

Grujic, D., Hollister, L., and Parrish, R., 2002, Himalayan metamorphic sequence as an orogenic channel: Insight from Bhutan: Earth and Planetary Science Letters, v. 198, p. 177–191, https://doi.org/10.1016/S0012-821X(02)00482-X.

Grujic, D., Warren, C.J., and Wooden, J.L., 2011, Rapid synconvergent exhumation of Miocene-aged lower and orogenic crust in the eastern Himalaya: Lithosphere, v. 3, p. 346–366, https://doi.org/10.1130/L154.1.

Guillope, M., and Poirier, J.P., 1979, Dynamic recrystallization during creep of single-crystalline halite: an experimental study: Journal of Geophysical Research. Solid Earth, v. 84, p. 5557–5567, https://doi.org/10.1029/JB084iB10p05557.

Harrison, T.M., Grove, M., Lovera, O.M., and Catlos, E.J., 1998, A model for the origin of Himalayan anatexis and inverted metamorphism: Journal of Geophysical Research. Solid Earth, v. 103, p. 27017–27032, https://doi.org/10.1029/98JB02468.

He, D., Webb, A.A., Larson, K.P., Martin, A.J., and Schmitt, A.K., 2015, Extrusion vs. duplexing models of Himalayan mountain building 3: Duplexing dominates from the Oligocene to Present: International Geology Review, v. 57, p. 1–27, https://doi.org/10.1080/00206814.2014.986669 (corrigendum: http://dx.doi.org/10.1080/00206814.2015.1005906).

Henry, P., LePichon, X., and Goffe, B., 1997, Kinematic, thermal and petrological model of the Himalayas: Constraints related to metamorphism within the underthrust Indian crust and topographic elevation: Tectonophysics, v. 273, p. 31–56, https://doi.org/10.1016/S0040-1951(96)00287-9.

Herren, E., 1987, Zanskar shear zone: Northeast-southwest extension within the Higher Himalayas (Ladakh, India): Geology, v. 15, p. 409–413, https://doi.org/10.1130/0091-7613(1987)15<409:ZSZNEW>2.0.CO;2.

Hodges, K.V., Parrish, R.R., Housh, T.B., Lux, D.R., Burchfiel, B.C., Royden, L.H., and Chen, Z., 1992, Simultaneous Miocene extension and shortening in the Himalayan orogen: Science, v. 258, p. 1466–1470, https://doi.org/10.1126/science.258.5087.1466.

Hodges, K.V., Parrish, R.R., and Searle, M.P., 1996, Tectonic evolution of the central Annapurna Range, Nepalese Himalayas: Tectonics, v. 15, p. 1264–1291, https://doi.org/10.1029/96TC01791.

Holyoke, C.W., and Tullis, J., 2006, Formation and maintenance of shear zones: Geology, v. 34, p. 105–108, https://doi.org/10.1130/G22116.1.

Hughes, N.C., Myrow, P.M., McKenzie, N.R., Harper, D.A.T., Bhargava, O.N., Tangri, S.K., Ghalley, K.S., and Fanning, C.M., 2011, Cambrian rocks and faunas of the Wachi La, Black Mountains, Bhutan: Geological Magazine, v. 148, p. 351–379, https://doi.org/10.1017/S0016756810000750.

Jamieson, R.A., Beaumont, C., Medvedev, S., and Nguyen, M.H., 2004, Crustal channel flows: 2. Numerical models with implications for metamorphism in the Himalayan-Tibetan orogen: Journal of Geophysical Research. Solid Earth, v. 109, no. B6, https://doi.org/10.1029/2003JB002811.

Jangpangi, B.S., 1978, Stratigraphy and structure of the Bhutan Himalaya, in Saklani, P.S., ed., Tectonic Geology of the Himalaya: New Delhi, India, Today's and Tomorrow's Publications, p. 221–242.

Johnson, S.E., Lenferink, H.J., Price, N.A., Marsh, J.H., Koons, P.O., West, D.P., Jr., and Beane, R., 2009, Clast-based kinematic vorticity gauges: The effects of slip at matrix/clast interfaces: Journal of Structural Geology, v. 31, p. 1322–1339, https://doi.org/10.1016/j.jsg.2009.07.008.

Kellett, D.A., and Grujic, D., 2012, New insight into the South Tibetan detachment system: Not a single progressive deformation: Tectonics, v. 31, no. 2, https://doi.org/10.1029/2011TC002957.

Kellett, D.A., Grujic, D., and Erdman, S., 2009, Miocene structural reorganization of the South Tibetan detachment, eastern Himalaya: Implications for continental collision: Lithosphere, v. 1, p. 259–281, https://doi.org/10.1130/L56.1.

Kellett, D.A., Grujic, D., Warren, C., Cottle, J., Jamieson, R., and Tenzin, T., 2010, Metamorphic history of a syn-convergent orogen-parallel detachment: The South Tibetan detachment system, Bhutan Himalaya: Journal of Metamorphic Geology, v. 28, p. 785–808, https://doi.org/10.1111/j.1525-1314.2010.00893.x.

Kellett, D.A., Cottle, J.M., and Larson, K.P., 2018, The South Tibetan Detachment System: History, advances, definition, and future directions, in Treloar, P.J., and Searle, M.P., eds., Himalayan Tectonics: A Modern Synthesis: Geological Society of London Special Publication 483, 24 p., https://doi.org/10.1144/SP483.2.

Kohn, M.J., 2008, P-T-t data from central Nepal support critical taper and repudiate large-scale channel flow of the Greater Himalayan Sequence: Geological Society of America Bulletin, v. 120, p. 259–273, https://doi.org/10.1130/B26252.1.

Kohn, M.J., 2014, Himalayan metamorphism and its tectonic implications: Annual Review of Earth and Planetary Sciences, v. 42, p. 381–419, https://doi.org/10.1146/annurev-earth-060313-055005.

Kohn, M.J., Wieland, M.S., Parkinson, C.D., and Upreti, B.N., 2004, Miocene faulting at plate tectonic velocity in the Himalaya of central Nepal: Earth and Planetary Science Letters, v. 228, p. 299–310, https://doi.org/10.1016/j.epsl.2004.10.007.

Kruhl, J.H., 1998, Prism- and basal-plane parallel subgrain boundaries in quartz: A microstructural geothermobarometer [Reply]: Journal of Metamorphic Geology, v. 16, p. 142–146.

Larson, K.P., and Cottle, J.M., 2014, Midcrustal discontinuities and the assembly of the Himalayan midcrust: Tectonics, v. 33, p. 718–740, https://doi.org/10.1002/2013TC003452.

Larson, K.P., Gervais, F., and Kellett, D., 2013, A P-T-t-D discontinuity in east-central Nepal: Implications for the evolution of the Himalayan mid-crust: Lithos, v. 179, p. 275–292, https://doi.org/10.1016/j.lithos.2013.08.012.

Larson, K.P., Ambrose, T.K., Webb, A.A.G., Cottle, J.M., and Shrestha, S., 2015, Reconciling Himalayan midcrustal discontinuities: The Main Central thrust system: Earth and Planetary Science Letters, v. 429, p. 139–146, https://doi.org/10.1016/j.epsl.2015.07.070.

Larson, K.P., Cottle, J., Lederer, G., and Rai, S.M., 2017, Defining shear zone boundaries using fabric intensity gradients: An example from the east-central Nepal Himalaya: Geosphere, v. 13, p. 771–781, https://doi.org/10.1130/GES01373.1.

Lavé, J., and Avouac, J.P., 2000, Active folding of fluvial terraces across the Siwaliks Hills, Himalayas of central Nepal: Journal of Geophysical Research. Solid Earth, v. 105, no. 3, p. 5735–5770, https://doi.org/10.1029/1999JB900292.

Law, R.D., 2010, Moine thrust zone mylonites at the Stack of Glencoul: II—results of vorticity analyses and their tectonic significance, in Law, R.D., Butler, R.W.H., Holdsworth, R., Krabbendam, M., and Strachan R.A., eds., Continental Tectonics and Mountain Building: The Legacy of Peach and Horne: Geological Society of London Special Publication, v. 335, p. 579–602, https://doi.org/10.1144/SP335.24.

Law, R.D., 2014, Deformation thermometry based on quartz c-axis fabrics and recrystallization microstructures: A review: Journal of Structural Geology, v. 66, p. 129–161, https://doi.org/10.1016/j.jsg.2014.05.023.

Law, R.D., Searle, M.P., and Simpson, R.L., 2004, Strain, deformation temperatures and vorticity of flow at the top of the Greater Himalayan Slab, Everest Massif, Tibet: Journal of the Geological Society, v. 161, p. 305–320, https://doi.org/10.1144/0016-764903-047.

Law, R.D., Jessup, M.J., Searle, M.P., Francsis, M.K., Waters, D.J., and Cottle, J.M., 2011, Telescoping of isotherms beneath the South Tibetan Detachment System, Mount Everest Massif: Journal of Structural Geology, v. 33, p. 1569–1594, https://doi.org/10.1016/j.jsg.2011.09.004.

Law, R.D., Stahr, D.W., Francsis, M.K., Ashley, K.T., Grasemann, B., and Ahmad, T., 2013, Deformation temperatures and flow vorticities near the base of the Greater Himalayan Series, Sutlej Valley and Shimla Klippe, NW India: Journal of Structural Geology, v. 54, p. 21–53, https://doi.org/10.1016/j.jsg.2013.05.009.

Leech, M.L., Singh, S., Jain, A.K., Klemperer, S.L., and Manickavasagam, R.M., 2005, The onset of India-Asia continental collision: Early, steep subduction required by the timing of UHP metamorphism in the western Himalaya: Earth and Planetary Science Letters, v. 234, p. 83–97, https://doi.org/10.1016/j.epsl.2005.02.038.

LeFort, P., 1975, Himalayas: The collided range, present knowledge of the continental arc: American Journal of Science, v. 275-A, p. 1–44.

Lister, G.S., 1977, Crossed-girdle c-axis fabrics in quartzite plastically deformed by plane strain and progressive simple shear: Tectonophysics, v. 39, p. 51–54, https://doi.org/10.1016/0040-1951(77)90087-7.

Lister, G.S., and Dornsiepen, U.F., 1982, Fabric transitions in the Saxony granulite terrain: Journal of Structural Geology, v. 4, p. 81–92.

Lister, G.S., and Hobbs, B.E., 1980, The simulation of fabric development during plastic deformation and its application to quartzite: The influence of deformation history: Journal of Structural Geology, v. 2, p. 355–370, https://doi.org/10.1016/0191-8141(80)90023-1.

Lister, G.S., and Williams, P.F., 1979, Fabric development in shear zones: Theoretical controls and observed phenomena: Journal of Structural Geology, v. 1, p. 283–297, https://doi.org/10.1016/0191-8141(79)90003-8.

Lister, G.S., Paterson, M.S., and Hobbs, B.E., 1978, The simulation of fabric development in plastic deformation and its application to quartzite: The model: Tectonophysics, v. 45, p. 107–158, https://doi.org/10.1016/0040-1951(78)90004-5.

Long, S., and McQuarrie, N., 2010, Placing limits on channel flow: Insights from the Bhutan Himalaya: Earth and Planetary Science Letters, v. 290, p. 375–390, https://doi.org/10.1016/j.epsl.2009.12.033.

Long, S., McQuarrie, N., Tobgay, T., and Grujic, D., 2011a, Geometry and crustal shortening of the Himalayan fold-thrust belt, eastern and central Bhutan: Geological Society of America Bulletin, v. 123, p. 1427–1447, https://doi.org/10.1130/B30203.1.

Long, S., McQuarrie, N., Tobgay, T., and Hawthorne, J., 2011b, Quantifying internal strain and deformation temperature in the eastern Himalaya: Implications for the evolution of strain in thrust sheets: Journal of Structural Geology, v. 33, p. 579–608, https://doi.org/10.1016/j.jsg.2010.12.011.

Long, S.P., McQuarrie, N., Tobgay, T., Grujic, D., and Hollister, L., 2011c, Geologic map of Bhutan: The Journal of Maps, v. 7, p. 184–192, scale 1:500,000, https://doi.org/10.4113/jom.2011.1159.

Long, S.P., Gordon, S.M., Young, J.P., and Soignard, E., 2016, Temperature and strain gradients through Lesser Himalayan rocks and across the Main Central thrust, south-central Bhutan: Implications for transport-parallel stretching and inverted metamorphism: Tectonics, v. 35, p. 1863–1891, https://doi.org/10.1002/2016TC004242.

Long, S.P., Gordon, S.M., and Soignard, E., 2017, Distributed north-vergent shear and flattening through Greater and Tethyan Himalayan rocks: Insights from metamorphic and strain data from the Dang Chu region, central Bhutan: Lithosphere, v. 9, p. 774–795, https://doi.org/10.1130/L655.1.

Mainprice, D.H., Bouchez, J.L., Blumenfeld, P., and Tubia, J.M., 1986, Dominant c slip in naturally deformed quartz: Implications for dramatic plastic softening at high temperature: Geology, v. 14, p. 819–822, https://doi.org/10.1130/0091-7613(1986)14<819:DCSIND>2.0.CO;2.

Mainprice, D., Bachman, F., Hielscher, R., and Schaeben, H., 2014, Descriptive tools for the analysis of texture projects with large datasets using MTEX: Strength, symmetry and components, in Faulkner, D.R., Mariani, E., and Mecklenburgh, J., eds., Rock Deformation from Field, Experiments and Theory: A Volume in Honour of Ernie Rutter: Geological Society of London, Special Publications, v. 409, p. 251–271, https://doi.org/10.1144/SP409.8.

Mattauer, M., 1986, Intracontinental subduction, crust-mantle décollement and crustal-stacking wedge in the Himalayas and other collision belts, in Coward, M.P., and Ries, A.C., eds., Collision Tectonics: Geological Society, London, Special Publication 19, p. 37–50.

McQuarrie, N., Long, S.P., Tobgay, T., Nesbit, J.N., Gehrels, G., and Ducea, M., 2013, Documenting basin scale, geometry and provenance through detrital geochemical data: Lessons from the Neoproterozoic to Ordovician Lesser, Greater, and Tethyan Himalayan strata of Bhutan: Gondwana Research, v. 23, p. 1491–1510, https://doi.org/10.1016/j.gr.2012.09.002.

Means, W.D., 1989, Stretching faults: Geology, v. 17, p. 893–896, https://doi.org/10.1130/0091-7613(1989)017<0893:SF>2.3.CO;2.

Means, W.D., 1994, Rotational quantities in homogeneous flow and the development of small-scale structures: Journal of Structural Geology, v. 17, p. 893–896.

Means, W.D., 1995, Shear zones and rock history: Tectonophysics, v. 247, p. 157–160, https://doi.org/10.1016/0040-1951(95)98214-H.

Means, W.D., Hobbs, B.E., Lister, G.S., and Williams, P.F., 1980, Vorticity and noncoaxiality in progressive deformation: Journal of Structural Geology, v. 2, p. 371–378, https://doi.org/10.1016/0191-8141(80)90024-3.

Morgan, S., and Law, R.D., 2004, Unusual transition in quartzite dislocation creep regimes and crystal slip systems in the aureole of the Eureka Valley-Joshua Flat-Beer Creek pluton, California: A case for anhydrous conditions created by decarbonation reactions: Tectonophysics, v. 384, p. 209–231, https://doi.org/10.1016/j.tecto.2004.03.016.

Murphy, M.A., and Yin, A., 2003, Structural evolution and sequence of thrusting in the Tethyan fold-thrust belt and Indus-Yalu suture zone, southwest Tibet: Geological Society of America Bulletin, v. 115, no. 1, p. 21–34, https://doi.org/10.1130/0016-7606(2003)115<0021:SEASOT>2.0.CO;2.

Najman, Y., Appel, E., Boudagher-Fadel, M., Bown, P., Carter, A., Garzanti, E., Godin, L., Han, J., Liebke, U., Oliver, G., Parrish, R., and Vezzoli, G., 2010, Timing of India-Asia collision: Geological, biostratigraphic, and paleomagnetic constraints: Journal of Geophysical Research. Solid Earth, v. 115, no. B12, https://doi.org/10.1029/2010JB007673.

Ojha, T.P., Butler, R.F., Quade, J., DeCelles, P.G., Richards, D., and Upreti, B.N., 2000, Magnetic polarity stratigraphy of the Neogene Siwalik Group at Khutia Khola, far western Nepal: Geological Society of America Bulletin, v. 112, p. 424–434, https://doi.org/10.1130/0016-7606(2000)112<424:MPSOTN>2.0.CO;2.

Passchier, C.W., 1987, Stable positions of rigid objects in non-coaxial flow: A study in vorticity analysis: Journal of Structural Geology, v. 124, p. 211–222.

Passchier, C.W., and Trouw, R.A.J., 2006, Microtectonics (2nd edition): New York, USA, Springer, 366 p.

Peternell, M., Russell-Head, D.S., and Wilson, C.J.L., 2011, A technique for recording polycrystalline structure and orientation during in situ deformation cycles of rock analogues using an automated fabric analyser: Journal of Microscopy, v. 242, p. 181–188, https://doi.org/10.1111/j.1365-2818.2010.03456.x.

Poirier, J.P., and Nicolas, A., 1975, Deformation-induced recrystallization by progressive misorientation of subgrain-boundaries, with special reference to mantle peridotites: The Journal of Geology, v. 83, p. 707–720, https://doi.org/10.1086/628163.

Powell, C.M., and Conaghan, P.J., 1973, Plate tectonics and the Himalayas: Earth and Planetary Science Letters, v. 20, p. 1–12, https://doi.org/10.1016/0012-821X(73)90134-9.

Rahl, J.M., Anderson, K.M., Brandon, M.T., and Fassoulas, C., 2005, Raman spectroscopic carbonaceous material thermometry of low-grade metamorphic rocks: Calibration and application to tectonic exhumation in Crete, Greece: Earth and Planetary Science Letters, v. 240, p. 339–354, https://doi.org/10.1016/j.epsl.2005.09.055.

Ramsay, J.G., 1967, Folding and Fracturing of Rocks: New York, USA, McGraw-Hill, 560 p.

Ramsay, J.G., 1980, Shear zone geometry: A review: Journal of Structural Geology, v. 2, p. 83–99, https://doi.org/10.1016/0191-8141(80)90038-3.

Ramsay, J.G., and Graham, R.H., 1970, Strain variation in shear belts: Canadian Journal of Earth Sciences, v. 7, p. 786–813, https://doi.org/10.1139/e70-078.

Ramsay, J.G., and Huber, M.I., 1983, Techniques of Modern Structural Geology, Vol. 1: Strain Analysis: London, UK, Academic Press, 307 p.

Ratschbacher, L., Frisch, W., and Liu, G., 1994, Distributed deformation in southern and western Tibet during and after the India-Asia collision: Journal of Geophysical Research, v. 99, p. 19917–19945, https://doi.org/10.1029/94JB00932.

Robinson, D.M., DeCelles, P.G., Garzione, C.N., Pearson, O.N., Harrison, T.M., and Catlos, E.J., 2003, Kinematic model of the Main Central Thrust: Geology, v. 31, p. 359–362, https://doi.org/10.1130/0091-7613(2003)031<0359:KMFTMC>2.0.CO;2.

Robinson, D.M., DeCelles, P.G., and Copeland, P., 2006, Tectonic evolution of the Himalayan thrust belt in western Nepal: Implications for channel flow models: Geological Society of America Bulletin, v. 118, p. 865–885, https://doi.org/10.1130/B25911.1.

Rowley, D.B., 1996, Age of initiation of collision between India and Asia: A review of stratigraphic data: Earth and Planetary Science Letters, v. 145, p. 1–13, https://doi.org/10.1016/S0012-821X(96)00201-4.

Sanderson, D.J., 1982, Models of strain variation in nappes and thrust sheets: A review: Tectonophysics, v. 88, p. 201–233, https://doi.org/10.1016/0040-1951(82)90237-2.

Schmid, S.M., and Casey, M., 1986, Complete fabric analysis of some commonly observed quartz c-axis patterns, in Hobbs, B.E., and Heard, H.C., eds., Mineral and Rock Deformation: Laboratory Studies: Washington, D.C., USA, American Geophysical Union, Geophysical Monograph Series, v. 36, p. 263–286, https://doi.org/10.1029/GM036p0263.

Searle, M.P., Simpson, R.L., Law, R.D., Waters, D.J., and Parrish, R.R., 2002, Quantifying displacement on the South Tibetan Detachment normal fault, Everest massif, and the timing of crustal thickening and uplift in the Himalaya and Tibet: Journal of Nepal Geological Society, v. 26, p. 1–6.

Searle, M.P., Simpson, R.L., Law, R.D., Parrish, R.R., and Waters, D.J., 2003, The structural geometry, metamorphic and magmatic evolution of the Everest massif, High Himalaya of Nepal-South Tibet: Journal of the Geological Society, v. 160, p. 345–366, https://doi.org/10.1144/0016-764902-126.

Searle, M.P., Law, R.D., Godin, L., Larson, K.P., Streule, M.J., Cottle, J.M., and Jessup, M.J., 2008, Defining the Himalayan Main Central thrust in Nepal: Journal of the Geological Society, v. 165, p. 523–534, https://doi.org/10.1144/0016-76492007-081.

Starnes, J.K., Long, S.P., Zhang, J., and Gordon, S.M., 2017, Using quartz petrofabric intensity parameters to delineate shear zones: A case study from the Main Central thrust in western Bhutan: Geological Society of America Abstracts with Programs, v. 49, no. 6, https://doi.org/10.1130/abs/2017AM-297707.

Stipp, M., Stunitz, H., Heilbronner, R., and Schmid, S.M., 2002, The eastern Tonale fault zone: A 'natural laboratory' for crystal plastic deformation over a temperature range from 250 to 700 °C: Journal of Structural Geology, v. 24, p. 1861–1884, https://doi.org/10.1016/S0191-8141(02)00035-4.

Tangri, S.K., and Pande, A.C., 1995, Tethyan sequence, in Bhargava, O.N., ed., The Bhutan Himalaya: A Geological Account: Geological Society of India Special Publication 39, p. 109–142.

Tikoff, B., and Fossen, H., 1993, Simultaneous pure and simple shear: The unifying deformation matrix: Tectonophysics, v. 217, p. 267–283, https://doi.org/10.1016/0040-1951(93)90010-H.

Tikoff, B., and Fossen, H., 1995, The limitations of three-dimensional kinematic vorticity analysis: Journal of Structural Geology, v. 17, p. 1771–1784, https://doi.org/10.1016/0191-8141(95)00069-P.

Tobgay, T., Long, S., McQuarrie, N., Ducea, M., and Gehrels, G., 2010, Using isotopic and chronologic data to fingerprint strata: The challenges and benefits of variable sources to tectonic interpretations, the Paro Formation, Bhutan Himalaya: Tectonics, v. 29, TC6023, https://doi.org/10.1029/2009TC002637.

Tobgay, T., McQuarrie, N., Long, S., Kohn, M.J., and Corrie, S., 2012, The age and rate of displacement along the Main Central Thrust in the western Bhutan Himalaya: Earth and Planetary Science Letters, v. 319–320, p. 146–158, https://doi.org/10.1016/j.epsl.2011.12.005.

Treagus, S.H., and Treagus, J.E., 2002, Studies of strain and rheology of conglomerates: Journal of Structural Geology, v. 24, p. 1541–1567, https://doi.org/10.1016/S0191-8141(01)00162-6.

Tullis, J., and Wenk, H.-R., 1994, Effect of muscovite on the strength and lattice preferred orientations of experimentally deformed quartz aggregates: Materials Science and Engineering, v. 175, p. 209–220, https://doi.org/10.1016/0921-5093(94)91060-X.

Urai, J.L., Means, W.D., and Lister, G.S., 1986, Dynamic recrystallization of minerals, in Hobbs, B.E., and Heard, H.C., eds., Mineral and Rock Deformation: Laboratory Studies: Washington, D.C., USA, American Geophysical Union, Geophysical Monograph Series, v. 36, p. 161–199.

Vollmer, F.W., 1990, An application of eigenvalue methods to structural domain analysis: Geological Society of America Bulletin, v. 102, p. 786–791, https://doi.org/10.1130/0016-7606(1990)102<0786:AAOEMT>2.3.CO;2.

Walker, J.D., Martin, M.W., Bowring, S.A., Searle, M.P., Waters, D.J., and Hodges, K.V., 1999, Metamorphism, melting and extension: Age constraints from the High Himalayan slab of Southeastern Zanskar and northwest Lahaul: The Journal of Geology, v. 107, p. 473–495, https://doi.org/10.1086/314360.

Wallis, S.R., 1992, Vorticity analysis in a metachert from the Sanbagawa Belt, SW Japan: Journal of Structural Geology, v. 14, p. 271–280, https://doi.org/10.1016/0191-8141(92)90085-B.

Wallis, S.R., 1995, Vorticity analysis and recognition of ductile extension in the Sanbagawa belt, SW Japan: Journal of Structural Geology, v. 17, p. 1077–1093, https://doi.org/10.1016/0191-8141(95)00005-X.

Warren, C.J., Grujic, D., Kellett, D.A., Cottle, J., Jamieson, R.A., and Ghalley, K.S., 2011, Probing the depths of the India-Asia collision: U-Th-Pb monazite chronology of granulites from NW Bhutan: Tectonics, v. 30, https://doi.org/10.1029/2010TC002738.

Waters, D.J., Law, R.D., Searle, M.P., and Jessup, M., 2018, Structural and thermal evolution of the South Tibetan Detachment shear zone in the Mt. Everest region, from the 1933 sample collection of L.R. Wager, in Ferrero, S., Lanari, P., Goncalves, P., and Grosch, E., eds., Metamorphic Geology: Microscale to Mountains Belts: Geological Society of London, Special Publication 478, 38 p., https://doi.org/10.1144/SP478.17.

Webb, A.A.G., 2013, Preliminary balanced palinspastic reconstruction of Cenozoic deformation across the Himachal Himalaya (northwestern India): Geosphere, v. 9, p. 572–587, https://doi.org/10.1130/GES00787.1.

Webb, A.A., Yin, A., Harrison, M.T., Celerier, J., and Burgess, P.W., 2007, The leading edge of the Greater Himalayan Crystalline complex revealed in the NW Indian Himalaya: Implications for the evolution of the Himalayan orogen: Geology, v. 35, p. 955–958, https://doi.org/10.1130/G23931A.1.

Webb, A.A.G., Schmitt, A.K., He, D., and Weigand, E.L., 2011, Structural and geochronological evidence for the leading edge of the Greater Himalayan Crystalline complex in the central Nepal Himalaya: Earth and Planetary Science Letters, v. 304, p. 483–495, https://doi.org/10.1016/j.epsl.2011.02.024.

White, S., 1977, Geological significance of recovery and recrystallization processes in quartz: Tectonophysics, v. 39, p. 143–170, https://doi.org/10.1016/0040-1951(77)90093-2.

White, S.H., Burrows, S.E., Carreras, J., Shaw, N.D., and Humphreys, F.J., 1980, On mylonites in ductile shear zones: Journal of Structural Geology, v. 2, p. 175–187, https://doi.org/10.1016/0191-8141(80)90048-6.

Whitney, D.L., and Evans, B.W., 2010, Abbreviations for names of rock-forming minerals: The American Mineralogist, v. 95, p. 185–187, https://doi.org/10.2138/am.2010.3371.

Wiesmayr, G., and Grasemann, B., 2002, Eohimalayan fold and thrust belt: Implications for the geodynamic evolution of the northwest Himalaya (India): Tectonics, v. 21, https://doi.org/10.1029/2002TC001363.

Wilson, C.J.L., Robinson, J., and Dugdale, A., 2009, Quartz vein fabrics coupled to elevated fluid pressures in the Stawell gold deposit, south-eastern Australia: Mineralium Deposita, v. 44, p. 245–263, https://doi.org/10.1007/s00126-008-0215-1.

Woodcock, N.H., 1977, Specification of fabric shapes using an eigenvalue method: Geological Society of America Bulletin, v. 88, p. 1231–1236, https://doi.org/10.1130/0016-7606(1977)88<1231:SOFSUA>2.0.CO;2.

Wu, C., Nelson, K.D., Wortman, G., Samson, S.D., Yongjun, Y., Jixiang, L., Kidd, W.S.F., and Edwards, M.A., 1998, Yadong cross structure and South Tibetan detachment in the east central Himalaya (89°–90°E): Tectonics, v. 17, p. 28–45, https://doi.org/10.1029/97TC03386.

Xypolias, P., Spanos, D., Chatzaras, V., Kokkalas, S., and Koukouvelas, I., 2010, Vorticity of flow in ductile thrust zones: Examples from the Attico-Cycladic Massif (Internal Hellenides, Greece), in Law, R.D., Butler, R.W.H., Holdsworth, R., Krabbendam, M., and Strachan, R.A., eds., Continental Tectonics and Mountain Building: The Legacy of Peach and Horne: Geological Society of London Special Publication, v. 335, p. 687–714, https://doi.org/10.1144/SP335.28.

Yin, A., 2006, Cenozoic tectonic evolution of the Himalayan orogen as constrained by along-strike variation of structural geometry, exhumation history, and foreland sedimentation: Earth-Science Reviews, v. 76, p. 1–131, https://doi.org/10.1016/j.earscirev.2005.05.004.

Yonkee, W.A., Czeck, D.M., Nachbor, A.C., Barszewski, C., Pantone, S., Balgord, E.A., and Johnson, K.R., 2013, Strain accumulation and fluid-rock interaction in a naturally deformed diamictite, Willard thrust system, Utah (USA): Implications for crustal rheology and strain softening: Journal of Structural Geology, v. 50, p. 91–118, https://doi.org/10.1016/j.jsg.2012.10.012.

Zeiger, K., Gordon, S.M., Long, S.P., Kylander-Clark, A.R.C., Agustsson, K., and Penfold, M., 2015, Timing and conditions of metamorphism and melt crystallization in Greater Himalayan rocks, eastern and central Bhutan: Insight from U-Pb zircon and monazite geochronology and trace-element analyses: Contributions to Mineralogy and Petrology, v. 169, no. 47, https://doi.org/10.1007/s00410-015-1143-6.